CZECH TECHNICAL UNIVERSITY IN PRAGUE
Faculty of Mechanical Engineering

Operational parameters of hybrid rocket motor with >10kN thrust

Pracovní parametry hybridního raketového motoru o tahu >10kN

MASTER THESIS

Author: Bc. Ľuboš Jiroušek
Supervisor: Mgr. Jaroslav Kousal, Ph.D.
Year: 2021

ZADÁNÍ DIPLOMOVÉ PRÁCE

I. OSOBNÍ A STUDIJNÍ ÚDAJE

Příjmení: **Jiroušek** Jméno: **Ľuboš** Osobní číslo: **437082**

Fakulta/ústav: **Fakulta strojní**

Zadávající katedra/ústav: **Ústav letadlové techniky**

Studijní program: **Letectví a kosmonautika**

Studijní obor: **Letadlová a kosmická technika**

II. ÚDAJE K DIPLOMOVÉ PRÁCI

Název diplomové práce:

Pracovní parametry hybridního raketového motoru o tahu >10kN

Název diplomové práce anglicky:

Operational parameters of hybrid rocket motor with >10kN thrust

Pokyny pro vypracování:

1) Proveďte rešerši pohonných látek a základních modelů procesu hoření v hybridních raketových motorech
2) Pro motor o tahu >10kN v principu použitelný pro sondážní raketu do mezosféry zvolte pohonné látky a navrhněte přibližný tvar zrna, komory a trysky
3) Nasimulujte průběh pracovních parametrů motoru v čase, tj. zejména průběh odhořívání paliva, teplotu, tlak, tah

Seznam doporučené literatury:

M. Chiaverini, K. Kuo, Fundamentals of Hybrid Rocket Combustion and Propulsion, AIAA, 2007, ISBN 978-1-56347-703-4
a další literatura dle doporučení vedoucího

Jméno a pracoviště vedoucí(ho) diplomové práce:

Mgr. Jaroslav Kousal, Ph.D., ústav letadlové techniky FS

Jméno a pracoviště druhé(ho) vedoucí(ho) nebo konzultanta(ky) diplomové práce:

Datum zadání diplomové práce: **30.04.2021** Termín odevzdání diplomové práce: **30.07.2021**

Platnost zadání diplomové práce: _____

Mgr. Jaroslav Kousal, Ph.D.	Ing. Robert Theiner, Ph.D.	prof. Ing. Michael Valášek, DrSc.
podpis vedoucí(ho) práce	podpis vedoucí(ho) ústavu/katedry	podpis děkana(ky)

III. PŘEVZETÍ ZADÁNÍ

Diplomant bere na vědomí, že je povinen vypracovat diplomovou práci samostatně, bez cizí pomoci, s výjimkou poskytnutých konzultací. Seznam použité literatury, jiných pramenů a jmen konzultantů je třeba uvést v diplomové práci.

. _____ _____

Datum převzetí zadání Podpis studenta

Prohlášení

Prohlašuji, že jsem svou diplomovou práci vypracoval samostatně a použil jsem pouze literaturu a informace, které cituji a uvádím v seznamu použité literatury a zdrojů.

V Praze dne ....

Bc. Ľuboš Jiroušek

Poděkování

Děkuji Mgr. Jaroslavovi Kousalovi, Ph.D. za vedení mé diplomové práce a za podnětné návrhy, které ji obohatily. Také děkuji rodině a přátelům za podporu a motivaci

Bc. Luboš Jiroušek

Název práce:
Pracovní parametry hybridního raketového motoru o tahu >10kN

Autor: Bc. Luboš Jiroušek

Studijní program: Letectví a kosmonautika
Obor: Letecká a kosmická technika
Druh práce: Master thesis

Vedoucí práce: Mgr. Jaroslav Kousal, Ph.D.

Bibliografické údaje: Počet stran: 49
Počet obrázků: 35
Počet tabulek: 7

Abstrakt: Cílem této práce je simulovat model nového středně velkého hybridního motoru s větším tahem, čím se myslí v desítkách kN. Model reprezentuje fyzikální vlastnosti motoru. Z modelu jsou pak určeny návrhové parametry, kterými jsou rozměry, hmotnost paliva, tlaky uvnitř motoru, tepelný tok, čas hoření a přesný průběh tahu na čase. Parametry budou pak použity jako vstup do konstrukčního návrhu motoru.
Klíčová slova: Hybridní raketový motor, Hybridní spalování,
Návrh raketového motoru, Parafín

Title:
Operational parameters of hybrid rocket motor with >10kN thrust

Author: Bc. Luboš Jiroušek

Abstract: The goal of this thesis is to simulate model of the new medium sized hybrid rocket motor with higher thrust, which is meant in tens of kN. The model represents physical properties of the motor. From the model are then determined design parameters, which are dimensions, fuel mass, pressures inside the motor, heat flow, burning time and the exact thrust relative to time. They will be then used as input in construction design of the motor.
Key words: Hybrid rocket motor, Hybrid combustion,
Rocket motor design, Paraffin

Contents

Nomenclature

a	Regression rate coefficient	$[-]$
a_t	Thickness parameter	$[m^2/s]$
B	Blowing parameter	$[-]$
c	Specific heat capacity	$[J/kg/K]$
c^*	Characteristic velocity	$[m/s]$
C_{B1}, C_{B2}	Blowing correction coefficients	$[-]$
C_F	Thrust coefficient	$[-]$
c_f	Skin friction coefficient	$[-]$
F	Thrust	$[N]$
G	Local mass flux	$[kg/m^2/s]$
G_o	Oxidizer mass flux	$[kg/m^2/s]$
h	Enthalpy	$[J/kg]$
h	Melt layer thickness	$[m]$
h_m, h_e	Total heats of melting and entrainment	$[J/kg]$
$\Delta H_{v,eff}$	Effective heat of vaporization	$[J/kg]$
I_{sp}	Specific impulse	$[Ns/kg]$
K	Concentration	$[-]$
K	Entrainment parameter constant	$[m^{4.4}s^{1.4}/kg^{2.4}]$
L	Latent heat	$[J/kg]$
L	Length of fuel grain	$[m]$
M	Molar mass	$[g/mol]$
$\dot{m}$	Mass flow rate	$[kg/s]$

m	Mass	$[kg]$
M_e	Exit mach number	$[-]$
n	Regression rate exponent	$[-]$
p_c, p_e	Chamber pressure and exit pressure of the nozzle	$[Pa]$
$\dot{q}$	Heat flux	$[W/m^2]$
R	Radius	$[m]$
$\dot{r}$	Regression rate	$[mm/s]$
Re	Reynolds number	$[-]$
R_{ent}	Entrainment parameter	$[-]$
St	Stanton number	$[-]$
T	Temperature	$[K]$
t	Time	$[s]$
u	Streamwise velocity component	$[m/s]$
z	Axial location	$[m]$

Greek Letters

δ	Characteristic thermal thickness	$[m]$
ϵ	Area ratio	$[-]$
γ	Specific heats ratio	$[-]$
λ	Thermal conductivity	$[W/m/K]$
μ	Viscosity	$[Ns/m^2]$
ϕ	Non-dimensonal regression rate	$[-]$
ψ	Thickness parameter	$[-]$
ρ	Density	$[kg/m^3]$

Subscripts

a	Ambient
c	Convective
cl	Classical
e	Boundary layer edge
ent	Entrainment

f	Final
f	Fuel
fl	Flame
g	Gas phase
i	Initial
l	Liquid phase
m	Melting
o	Oxidizer
r	Radiative
s	Solid phase
tot	Total
v	Vaporization
w	Wall

Introduction

Chemical propulsion systems can be categorized into three major groups based on the phase state of their propellants. Propellants of chemical rocket engines consists of oxidizer and fuel. First group are liquid rocket engines, where both propellants are in liquid state. Second group are solid rocket motors, where both propellants are mixed together in solid state. Third group are hybrid rocket motors, where one propellant is in solid state stored in combustion chamber and other in liquid state stored in a tank. Hybrid rocket motors are divided based on configuration of their propellants into classical, where oxidizer is in liquid state and fuel is in solid state or inverse, where it's opposite. Classical hybrids are more widely used than inverse, so the focus will be on them.

In classical hybrids, typically cylindrical solid fuel grain with single or multiple ports is stored already in combustion chamber where it burns with oxidizer through its ports. Liquid (or gaseous) oxidizer is stored in a tank which is located above combustion chamber. Oxidizer tank can be pressurised by helium. Oxidizer is fed into the combustion ports either by a gas pressure or by a pump system. Oxidizer flow is controlled by a valve. Oxidizer is then injected through injector to create uniform flow and is ignited. The hot gases created by combustion are then expanded through the nozzle to generate thrust.

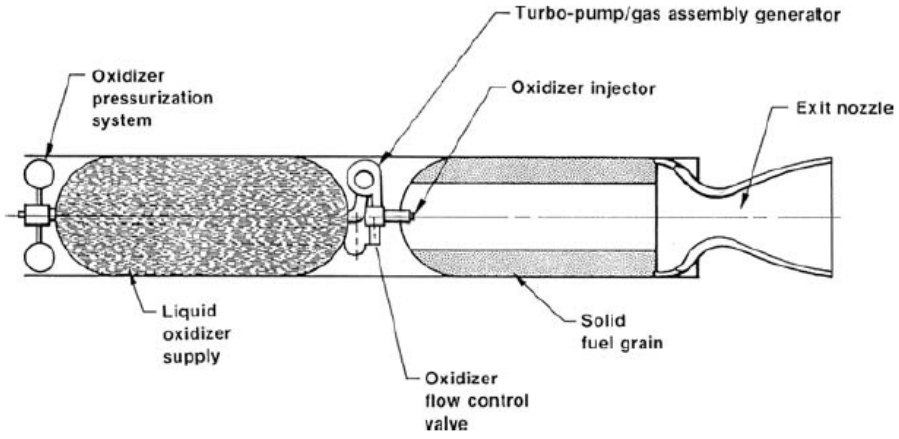

Figure 1: Scheme of classical hybrid rocket motor [1]

Unlike liquid and solid rockets, hybrid rockets are the least developed and there is potential for significant improvements and as an option for specific future generation propulsion systems. Hybrid rocket motors are so far mostly used in academic sphere by universities. Only commercial use is by company Virgin Galactic in suborbital spacecraft SpaceShipOne and SpaceShipTwo that just recently successfully flew with the crew. In recent years there's been big interest in using hybrid rocket mo-

tors for medium sized sub-orbital sounding rockets and companies and universities started to develop and build their own medium sized hybrid motors. For example in Taiwan is being developed two-stage suborbital hybrid rocket Hapith I, which should be able to reach maximum height of 308 km. [2] Thrust of these rockets is in tens of kN.

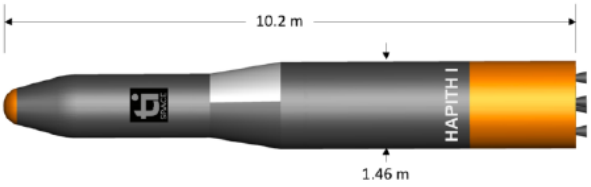

Figure 2: Hapith I suborbital launch vehicle [2]

Advantages and Disadvantages

As hybrid rockets differ from liquid and solid rockets, they hold number of advantages and disadvantages. The main advantages are:

1) Safety: By storing solid fuel and liquid oxidizer separately, there is no risk of explosion, as it is at solid rockets, where oxidizer and fuel are mixed together. Hybrid rocket propellants are then non-explosive and non-toxic so they can be manufactured, transported, and handled safely.

2) Simplified throttling: Throttling can be regulated by regulating oxidizer flow with control valve. Decrease of oxidizer flow will decrease evaporation of fuel and it decreases thrust. Motor can be also completely shut down and then reignited. Compared to liquid rockets it doesn't need synchronization of fuel and oxidizer flow.

3) Non-sensitivity to cracks: Burning of fuel occurs only where where it encounters the oxidizer flow, which means it doesn't depend on pressure as solid rockets are. Cracks in fuel are then non-catastrophic.

4) High performance: Hybrid rockets have higher I_{sp} than solid rockets. Propellants LOX and HTPB have vacuum specific impulse almost 360 s (3531 Ns/kg) which is comparable to liquid bipropellant LOX/RP-1. [3] Since hybrids need only half of turbo-machinery than liquid rockets, they have less weight and density specific impulse is higher than liquids.

5) Low cost: Safety features also causes low cost for manufacture and handling of propellants. Also thanks to small complexity, fabrication cost of the motor is low.

Also, there are some disadvantages:

1) Low regression rate: To have higher thrust requires higher mass of fuel to be burned, which means larger fuel surface area. By increasing inner diameter, regression rate is lower. This problem is solved either by creating multiple ports in combustion chamber that provide adequate burning surface and higher regression rate or using solid propellant that liquefy on surface.

2) Combustion efficiency: As burning oxygen flows through combustion chamber, it doesn't mix properly with fuel, therefore resulting in a lower impulse efficiency.

3) O/F shift: As the area of the port is increasing during burning time, burning surface increases, but regression rate decreases faster, so fuel mass flow rate decreases which causes oxidizer/fuel ratio to slightly shifts higher, which lowers the motor performance.

Chapter 1

Theory

In this chapter will be discussed various theories and analyses about how hybrid rocket motors work. It includes propellants that were tested and can be used, process of combustion and different theoretical models. Most of the classical theory is introduced in book *Fundamentals of Hybrid Rocket Combustion and Propulsion* by CHIAVERINI, Martin J.; KUO, Kenneth K [1][4][5] and combustion of paraffin waxes in Ref. [6] and [7]

1.1 Typical fuels and oxidizers

Compared to liquid and solid rockets, hybrid rockets have large variety of combinations of fuels and oxidizers because two phases are available. Classical hybrids have the largest number of possible propellants combinations, where oxidizers are easier to store in liquid or gaseous state and there is also large number of possible solid fuels. Inverse hybrids have problem to have oxidizer in solid form, as they are either less effective than liquid or there is problem storing them in cryogenic form. Fuels in liquid form also pose danger of explosion.

Inert solid fuels are generally hydrocarbons that burn with oxygen. Best performance and mechanical properties have natural rubbers and polymeric synthetic rubbers based on the polybutadiene monomer (PB). The most popular, based on cost and commercial availability, is HTPB (hydroxyl-terminated polybutadiene). Other hydrocarbons that have been used, are the paraffin waxes, polyethylene (a higher molecular weight version of paraffin), Plexiglas (PMMA), metatoluene diamine/nylon, and, in earlier small-scale testing, the common fuels, coal and wood. [4] Plexiglas is mostly used in small laboratory scale motors.

Disadvantage of classical hybrid motor fuels and especially rubbers as HTPB is low burning rate, which means it has problem to create high thrust. To increase thrust and burning rate, certain metal additives can be used to increase weight and radiation heat transfer to the fuel. Common additive metal is nano-sized aluminium powder. [4] It will although slightly decrease specific impulse I_{sp}. Next option is to create multiple ports in fuel grain that will have smaller cross section area and increase burning area. Downside is then leftover fuel slivers after burn and also web support for the ports that create extra weight.

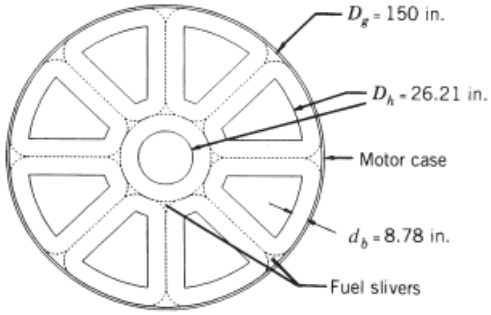

Figure 1.1: Example of multi-port fuel grain [8]

Another option how to increase burning rate is to use paraffin (wax) based fuels where burning rate is 3-4 times higher than that of conventional HTPB. [9] They belong to group of normal alkanes which are fully saturated, straight chain hydrocarbons with the chemical formula C_nH_{2n+2}. They are identified by the carbon number n, which goes from 1 (methane) up. The high heat of combustion (due to the high hydrogen to carbon ratio), low cost, availability and chemical inertness characteristics of n-alkanes makes them ideal fuels for combustion systems. Paraffin waxes have carbon number n from about 16 to 40. Another alkane of the interest is pentane (n=5), that is naturally liquid, so it has to be kept in cryogenic temperature using liquid nitrogen with temperature 77 K. Other alkanes are Polyethylene (PE) waxes (n=40-300) and High Density Polyethylene (HDPE) polymer (n>300). [6] These are naturally in solid state so they don't need to be cooled down. Pentane is used as pure n-alkane, but most of other fuels with higher carbon number, as Paraffin and Polyethylene waxes are used as mixtures of n-alkanes with different carbon numbers, because as pure they have bad mechanical properties (they are brittle). Their carbon number is then calculated as number average. In polymer science is used useful concept, polydispersity (PD), which is the ratio of the weight average carbon number to to the number averaged carbon number. For example Paraffin wax FR5560 has number averaged carbon number 32 and polydispersity 1.1. [6]

Liquid oxidizers are the same as in liquid rocket engines. The most commonly used oxidizer is liquid or gaseous oxygen (LOX or GOX) because of its high oxidation potential and therefore it has the highest specific impulse from all other oxidizers. [4] Another oxidizers also used are N_2O, N_2O_4, H_2O_2 and FLOX (2/3 F_2 + 1/3 O_2). Nitrous oxide (N_2O) has been tested in smaller scale motors [10], where was proven its lower specific impulse. FLOX is an experimental high energetic oxidizer that has been developed by NASA in 1960s. [4] It hasn't been well used yet in practical use because of toxicity of its combustion products, especially hydrofluoric acid (HF).

In table 1.1 are shown common fuel and oxidizer combinations from which will be selected best suitable combination for designed motor. In Figure 1.2 is plotted theoretical characteristic velocity c^* as a function of oxidizer to fuel ratio for different combinations of propellants mentioned above.

Fuel	Oxidizer	Optimum O/F	Sea level I_{sp} [Ns/kg]	c^* [m/s]
HTPB	LOX	1.9	2746.8	1820.3
HTPB	FLOX(OF_2)	3.3	3080.3	2042.5
Paraffin	LOX	2.5	2756.6	1804.4
Paraffin	N_2O	8	2432.9	1605.7
HTPB/Al(60%)	FLOX(OF_2)	2.5	3060.7	2006.2

Table 1.1: Performance of hybrid propellants, $p_c = 3.45\ MPa$ and $p_e = 1\ atm$ [4]

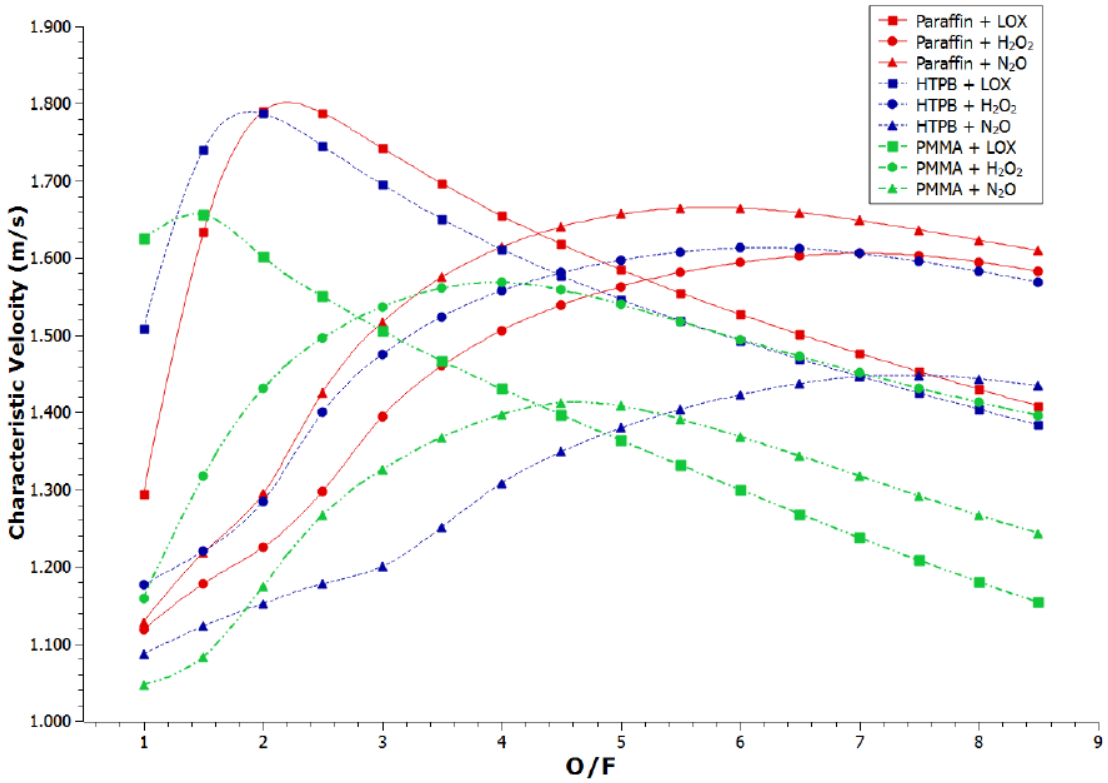

Figure 1.2: Characteristic velocity c^* as a function of oxidizer to fuel ratio for different combinations of propellants [11]

1.2 Combustion process and regression rate

Combustion in hybrid rockets doesn't occur directly on the surface of the fuel, but in a turbulent boundary-layer created by oxidizer flow as shown in Figure 1.3. Boundary-layer is assumed to be turbulent due to the high Reynolds number of the oxidizer flow and also due to the destabilizing influence of mass injection at the solid surface. Boundary-layer is split into three zones. One is a flame zone, where concentrations of oxidizer and fuel are sufficient for combustion to occur. Flow below flame zone is fuel rich, where normal gradient of temperature is in the same direction and flow above flame zone is oxidizer rich and gradient of temperature is in the opposite direction. Heat from the flame zone is transferred by convection and radiation to the solid fuel surface. The flame zone is located at approximately 10–20 % of the boundary-layer thickness above the surface. This theoretical model of boundary-layer combustion was first introduced by Marxman and Gilbert in 1962. [1]

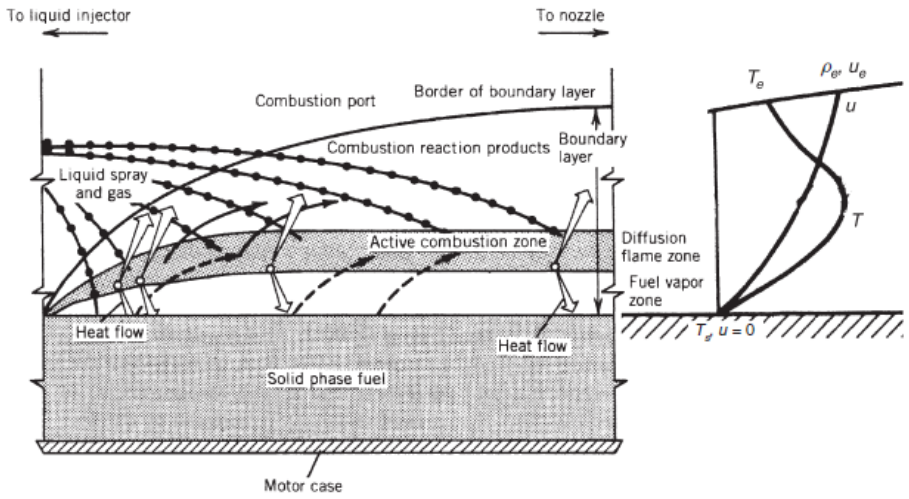

Figure 1.3: Model of boundary-layer in combustion chamber [8]

Combustion in rocket engine is most efficient when it occurs in certain optimal O/F ratio, which is a ratio of oxidiser mass flow rate $\dot{m}_o$ to fuel mass flow rate $\dot{m}_f$. Efficiency of combustion in rocket motors is represented by characteristic velocity c^*, which reflects the propellants energy, and specific impulse I_{sp}, which can be described as produced thrust from 1 kg of propellants per second and can be calculated as total thrust F over total propellants mass flow rate $\dot{m}_p$ and it also equals escape velocity v_e. Optimal O/F ratio doesn't always have to be equal to stoichiometric ratio of oxidizer and fuel and it's already found by experiments for each combination of propellants, which is shown in Table 1.1. When O/F ratio shifts higher from optimal during the burn, combustion efficiency decreases.

The key parameter for designing hybrid rocket motor is regression rate $\dot{r}$, which represents how fast fuel is converted from a solid-phase to a gas. Units of regression rate are in mm/s. Solid fuel converts to a gas either directly by sublimation, which is a phase transition from a solid to gas without entering liquid phase or by pyrolysis, "a solid-to-gas phase change that is accompanied by a chemical change, such as the polymer chain breaking, cyclization, and re-organization that occurs in the in-depth near-surface region when polymer-based fuels degrade and regress." [1] Vaporised fuel is then transported to the flame zone by convection and diffusion, that's why it's also called diffusion flame zone. There it mixes and chemically react with gaseous oxidizer which has been transported through the boundary layer from the core flow region via turbulent diffusion. Heat from the chemical reaction then sustain further pyrolysis, which is also called as wall blowing effect. However, the fuel mass flux due to pyrolysis blocks some of the heat transfer to the surface, which causes a decrease in the regression rate, which in turn, weakens the blocking action, so again more heat reaches the surface, and so on. This tendency toward a self-regulating interaction between heat flux, mass blowing, and heat flux blockage is a distinguishing characteristic of hybrid combustion. [1]

Paraffin waxes have slightly different process of burning, where they create melted liquid layer on the surface, that then spray droplets into the gas flow. This special process will be discussed later, because the combustion is similar as in classical polymer based fuels.

1.2.1 Heat-transfer-limited theory,

To optimize the design of high-performance hybrid motor, it is important to understand the physical processes that govern solid-fuel regression. Internal ballistics of the hybrid motor is very complex and it can't be precisely modelled with simple equations. There are multiple theories how to analyse regression rate in hybrid motors. The most influential is by Marxman and Gilbert. Their analysis is based on experiments they did mostly on HTPB fuel. Based on their theory, also called heat-transfer-limited theory, regression rate of solid fuel is governed by heat flux convected and radiated from the flame zone to the surface. The energy flux balance at the fuel surface can be expressed as

$$\dot{q}_{tot} = \rho_f \dot{r} \Delta H_{v,eff} \tag{1.1}$$

where ρ_f is solid fuel density in $[g/cm^3]$ and $\Delta H_{v,eff}$ is the effective heat of gasification of the solid fuel which is total energy required to heat a unit mass of the solid fuel from its initial temperature and then to vaporize it. This equation states that the enthalpy delivered to the fuel surface via solid-fuel regression equals the total heat flux incident on the fuel surface and also that product of solid-fuel density and regression rate must equal to the pyrolyzed-fuel mass flux. [1]

In classical hybrids using only polymers without metal additives, heat transfer by convection is dominating and radiative heat flux can be neglected. By assuming turbulent boundary-layer along the whole length of fuel grain, Marxman and Gilbert expressed total heat flux and developed an equation for the local solid-fuel regression rate given by

$$\rho_f \dot{r} = CGRe_x^{-0.2}(St/St_0)(u_e/u_{fl})[(h_{fl} - h_w)/\Delta H_{v,eff}] \tag{1.2}$$

where C is a function of the mainstream Mach number (about 0.03 for the low Mach numbers encountered in hybrids), $G = (\dot{m}_o + \dot{m}_{f,loc})/A_p$ is the local mass flux due to both oxidizer injection and all upstream fuel addition, where A_p is port cross section area, its units are in $[kg/m^2/s]$. The ratio of Stanton numbers, St/St_0, also referred as blocking factor, represents the fraction of heat transferred to the surface by convection when compared to the case with no wall blowing (no blocked heat). Typically its value is lower than 0.2. u_e/u_{fl} is the ratio of gas stream velocity at the edge of the boundary-layer to the velocity at the flame zone. Marxman et al. showed that the velocity ratio is determined by the flame position in the boundary layer and that it may be obtained by using the integral technique of boundary-layer theory and can be expressed as [1]

$$\frac{u_e}{u_{fl}} = \frac{K_{o_e} + (K_{o_e} + O/F_{fl})[(h_{fl} - h_w)/\Delta H_{v,eff}]}{O/F_{fl}[(h_{fl} - h_w)/\Delta H_{v,eff}]} \tag{1.3}$$

where K_{ox_e} is oxidizer concentration at the edge of boundary-layer which is for oxygen 1, $(h_{fl} - h_w) = \Delta h$ is the stagnation enthalpy difference between the flame zone and the surface (wall). O/F_{fl} is the oxidizer to fuel ratio at the flame zone and together with the $(h_{fl} - h_w)/\Delta H_{v,eff}$ factor are assumed to be independent of axial location and to be constant for certain oxidizer/fuel combination.

Wall blowing (fuel pyrolysis) is represented by blowing number B and is expressed as

$$B = (u_e/u_{fl})[(h_{fl} - h_w)/\Delta H_{v,eff}] = \frac{K_{o_e} + (K_o + O/F_{fl})\Delta h/\Delta H_{v,eff}}{O/F_{fl}} \tag{1.4}$$

Blowing number is an important parameter for estimation of regression rate and can be described as a thermodynamic parameter of the system that describes the enthalpy driving force between the flame and the wall that causes fuel regression.

Ratio of Stanton numbers was approximated by Marxman and later adjusted by Altman as a function of B for $5 < B < 100$

$$\frac{St}{St_0} = 1.2B^{-0.68} \tag{1.5}$$

As blowing number increases, more heat gets blocked to the surface, which will decrease St/St_0.

By combining Equations 1.2, 1.4 and 1.5 is obtained regression rate expression for hybrid combustion with no radiant heat transfer [8]

$$\dot{r} = 0.036\frac{G^{0.8}}{\rho_f}\left(\frac{\mu_g}{x}\right)^{0.2} B^{0.32} \tag{1.6}$$

where μ_g is viscosity of combustion gas. From Eq. 1.6 can be seen, that regression rate is strongly dependent on mass flux G and rather weakly on blowing effect B and axial location x. Also in normal regime, regression rate doesn't depend on chamber pressure. As fuel burns, port diameter and therefore also burning surface is increasing, port area is thereby increasing by R^2 so mass flux is decreasing faster and so regression rate is decreasing exponentially by time.

Oxidizer mass flow rate $\dot{m}_o$ is an input parameter for the combustion process and can be directly changed. When assuming certain fixed port radius, then by changing the size of the oxidizer flow rate, it will change by the same amount also oxidizer flux which can be expressed as

$$G_o = \dot{m}_o/(\pi R^2) \tag{1.7}$$

Total mass flux can be expressed also as $G = G_o(O/F + 1)/O/F$. Eq. 1.6 can be practically used only for certain range of mass fluxes, which is called "normal" regression rate regime that is showed in the middle of the Figure 1.4. So then oxidizer mass flow rate and oxidizer flux have to be in certain intermediate range as well. The upper limit is called "flooding" limit, where oxidizer flux is high enough so it will start to extinguish fire in the flame zone and decrease heat. It appears to depend on specific fuel/oxidizer combination and chamber pressure. Lower limit is then called "melting limit", when oxidizer flux is so low, which causes low convective heat to the surface, therefore, low regression rates and the heat transferred by radiation starts to be more significant and regression rate starts to be more dependent on chamber pressure. Depending on the specific type of fuel, this situation can lead to melting or charring and subsurface cooking reactions that may cause the virgin fuel to undergo depolymerization reactions well below the surface. [1]

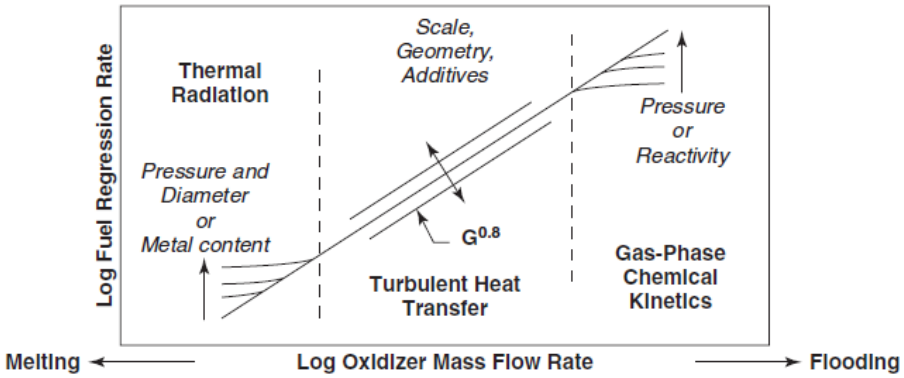

Figure 1.4: Regimes of regression rate depending on oxidizer flux [8]

1.2.2 Liquid layer combustion theory

In this section will be explained liquid layer combustion theory developed by Karabeyoglu et al. [6][12] that will be able to predict the regression rate performance of selected fuel that creates low viscosity liquid layer on burning surface. Firstly it was developed for cryogenic propellants, such as Pentane, but it also works for non-cryogenic materials such as Paraffin waxes. During experiments with different propellants was found, that normal alkanes burn with 3-4 times higher regression rate than classical HTPB. One explanation could be, that it is caused by lower effective heat of gasification $\Delta H_{v,eff}$ that is in classical regression Eq. 1.6 incorporated in blowing parameter B, raised to power 0.32. Therefore increase in regression rate would only be by 30 - 50 %. It was found that in addition to the classical gasification, these propellants create low viscosity liquid layer on burning surface that is hydrodynamically unstable in a strong gas flow and it causes a mass entrainment of liquid droplets into the gas stream which is shown in Figure 1.5. The reason of the instability is low viscosity of liquid layer of the propellant.

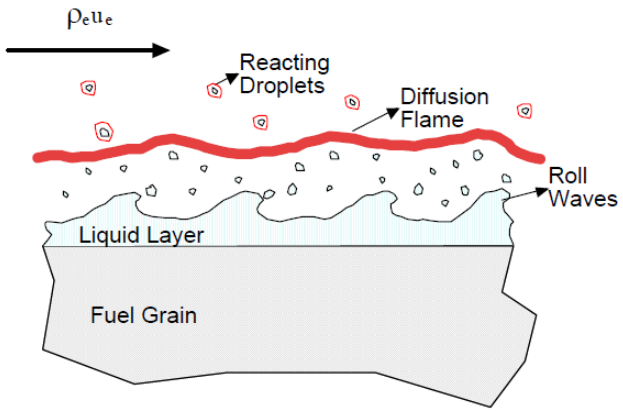

Figure 1.5: Schematic of the entrainment mechanism [6]

Because of the complexity of the problem, approach of the theory is split into three steps. First step is to investigate the requirements for the formation of a melt layer on the fuel grain. In the second, the linear stability of a thin melt layer under the strong shear of a gas flow is being considered, of which results are then linked to the entrainment of liquid droplets. Finally then classical heat-transfer limited theory is adjusted because of the effect of the entrainment.

Depending on critical pressure of material and combustion chamber pressure p_c, fuel burns either in subcritical or supercritical regime. In subcritical regime, fuel directly evaporates from liquid layer. In supercritical, the thermodynamic distinction between the liquid and gas phase is lost and above liquid layer is pyrolysis layer, where fuel is as supercritical fluid which then enters gas stream and burns in the flame zone. Surface temperature is then in subcritical regime determined by evaporation phenomenon and is sensitive to the chamber pressure, and in supercritical regime it depends on the pyrolysis chemical reactions and is not dependent on pressure. With increasing carbon number, critical pressure is decreasing and in infinity it asymptotes to zero. In typical hybrid motor chamber pressures, Pentane burns subcritically and Paraffin waxes as n-alkanes with carbon number higher than 16 burn supercritically. In pyrolysis process in supercritical condition paraffin decompose to ethylene and hydrogen which can be written as [7]

$$C_{32}H_{66} \longrightarrow 16C_2H_4 + H_2 \tag{1.8}$$

Generally, total regression rate can be written as sum of vaporization component $\dot{r}_v$, determined by vaporisation or pyrolysis and entrainment component $\dot{r}_{ent}$, characterised by mechanical transfer of liquid droplets.

$$\dot{r} = \dot{r}_v + \dot{r}_{ent} \tag{1.9}$$

The thickness of the liquid layer is determined by the convective and radiative heat transfer as seen in Figure 1.6. The thermophysical properties of the material both in the liquid phase and solid phase are assumed to be uniform. Fuel slab is split into two zones. On the surface is thin liquid layer and in the supercritical regime pyrolysis zone with supercritical fluid, where some part of fuel is already in vapor state. Parameter Y represents fraction of liquid fuel to the total fuel mass. The temperature varies from the wall temperature T_w to the melting temperature T_m. Underneath is solid zone, where the temperature decreases from T_m to ambient temperature T_a at infinite distance from the surface. The derivation was done using energy balance at the phase interfaces, such as gas-liquid and liquid-solid. It has been assumed for subcritical regime, but it's been proven that it is also valid for supercritical. The thermal analysis then yielded the following expression for the thickness of the melt layer [6]

$$h = \delta_l ln(1/\psi) \tag{1.10}$$

where δ_l is the characteristic thermal thickness in the liquid phase defined as

$$\delta_l = \frac{\kappa_l \rho_l}{\dot{r}\rho_f} = \frac{\lambda_l}{\dot{r}c_l\rho_f} \tag{1.11}$$

where λ_l is thermal conductivity of liquid fuel, c_l is specific heat capacity of liquid phase and ρ_l is density of liquid. ψ is the thickness parameter, that depends mainly on the thermophysical properties and radiative absorption character of the fuel and the nature of the heat transfer to the fuel surface. The effect of the radial convection in the liquid layer is ignored because of both the small melt layer thicknesses and low liquid vertical velocity. For convenience, following definitions of the effective heating parameters are introduced

$$h_m = L_m + c_s(T_m - T_a) \tag{1.12}$$

$$h_e = h_m + c_l(T_w - T_m) \tag{1.13}$$

$$\Delta H_{v,eff} = h_e + L_v(\dot{r}_v/\dot{r}) \tag{1.14}$$

L_m and L_v are the heat of melting and vaporisation respectively. T_a, T_m and T_s are the ambient, melting and surface temperatures of the fuel, respectively.

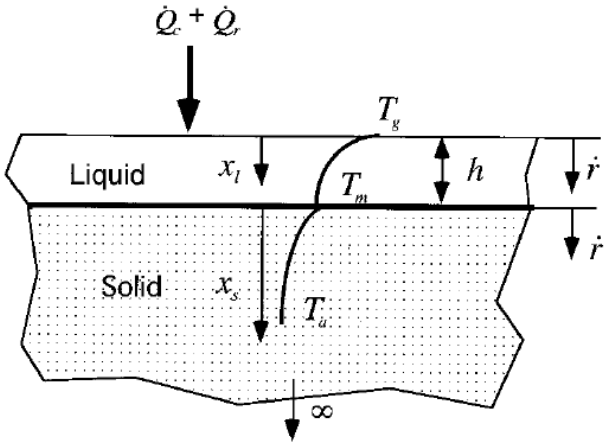

Figure 1.6: Schematic of the thermal model used in the melt layer thickness estimation [12]

Solution for the thickness parameter exists for two extreme cases. First case is where the absorption of the radiation in the liquid layer is very large. Thickness of the liquid layer can then be expressed as

$$h = \delta_l ln[1 + c_l(T_s - T_m)/h_m] \tag{1.15}$$

All the radiative heat is absorbed in the gas-liquid interface. This can be accomplished by adding strongly absorbing material to the fuel, such as carbon black powder.

Second case is when the absorption of the radiation in the liquid layer is very small and all the radiative heat is absorbed in the solid. This case has practical importance for cryogenic hybrids such as pentane which were tested without a radiation absorption agent.

$$h = \delta_l ln\left[1 + \frac{c_l(T_s - T_m)}{h_m - \Delta H_{v,eff}(\dot{q}_r/\dot{q}_{tot})}\right] \tag{1.16}$$

In this case liquid layer thickness is dependent on the entrainment mass transfer that comes from effective heat of gasification and ratio of radiative heat flux to the total heat flux.

Since liquid layer thickness is dependent on regression rate, independent thickness parameter is introduced.

$$a_t = h\dot{r} = \frac{\lambda_l}{c_l\rho_f} ln(1/\psi) \tag{1.17}$$

From experiments of strong blowing on thin liquid layers was developed formula for mass entrainment per unit area.

$$\dot{m}_{ent} = \dot{r}_{ent}\rho_f = K\frac{c_f h^\beta \rho_l G^{2\alpha}}{\mu_l} = K\frac{c_f a_t^\beta \rho_l}{\mu_l}\frac{G^{2\alpha}}{\dot{r}^\beta} \tag{1.18}$$

K is the empirical entrainment parameter constant, that is only parameter that can be freely adjusted to match experimental data, c_f is skin friction coefficient, dynamic pressure exponent α and the thickness exponent β are selected as 1.5 and 2 respectively. [6] As can be seen, entrainment regression rate depends both on operational parameters, as local total mass flux G and total regression rate $\dot{r}$, and on liquid fuel properties as its viscosity, density and thickness parameter. By dividing solid fuel density on right side, liquid fuel properties can be introduced as entrainment coefficient a_{ent}, where skin friction coefficient c_f can be included into parameter K.

$$\dot{r}_{ent} = a_{ent}\frac{G^3}{\dot{r}^2} \quad \text{and} \quad a_{ent} = K\frac{a_t^{\beta}\rho_l}{\mu_l \rho_f} \tag{1.19}$$

Modification of the Classical Theory for Entrainment: Instability of liquid layer and entrainment of liquid droplets causes three major modifications to the classical heat-transfer-limited theory. First is, that the effective heat of gasification is reduced as heat of vaporization is only needed for vaporization regression rate component, which can be seen in Eq. 1.14 that is derived from following relation.

$$\dot{q}_{tot} = h_e \rho_f \dot{r} + L_v \rho_f \dot{r}_v = \Delta H_{v,eff} \rho_f \dot{r} \tag{1.20}$$

Also enthalpy difference between surface and flame zone is reduced, because there are liquid droplets. This reduction is smaller than reduction of $\Delta H_{v,eff}$, therefore the reduction in the flame enthalpy is assumed to be negligible.

Second modification is, that the blocking factor St/St_0 is altered because of the two-phase flow. First approximation is, that the effect of liquid droplets on the momentum and energy transfer is being ignored. Therefore blocking factor is only a function of evaporation blowing number B_g, that only includes the gaseous phase mass transfer from the fuel surface.

$$St/St_0 = f(B_g) \tag{1.21}$$

As B_g is small, Eq. 1.5 can not be used as the blocking factor gets even larger than one. Second approximation is, that evaporation of the droplets released from the liquid surface into the gas stream does not take place beneath the flame sheet. This is due to high blowing rates, therefore there is low residence time of droplets between the liquid surface and the diffusion flame.

Third modification is, that the ripples formed on the liquid layer surface increase the surface roughness, therefore the heat transfer from the flame front to the surface. This has although smaller influence than previous two.

For calculation of total regression rate, the energy balance at the liquid-gas interface is estimated as

$$\dot{r}_v + [R_{he} + R_{hv}(\dot{r}_v/\dot{r})]\dot{r}_{ent} = F_r \frac{0.03\mu_g^{0.2}}{\rho_f}(1 + \dot{q}_r/\dot{q}_c)B\frac{St}{St_0}G^{0.8}z^{-0.2} \tag{1.22}$$

where R_{he} and R_{hv} are the non-dimensional energy parameters for entrainment and vaporization respectively, described as

$$R_{he} = \frac{h_m}{\Delta H_{v,eff}} \quad \text{and} \quad R_{hv} = \frac{c_l(T_s - T_m)}{\Delta H_{v,eff}} \tag{1.23}$$

F_r is the roughness parameter that accounts for the increased heat transfer by wrinkling of the liquid surface. Since it is relatively small, it is assumed to be unity.

The right side of Eq. 1.22 is similar to Eq. 1.6, but here is also included radiative heat flux $\dot{q}_r$. From experiments was radiative to convective heat flux ratio $\dot{q}_r/\dot{q}_c$ estimated to be 0.1.

New curve fit for Eq. 1.21 was given in Ref. [12] as

$$\frac{St}{St_0} = \frac{2}{2 + 1.25B_g^{0.75}} = \frac{C_{B1}}{C_{B1} + C_{B2}(\dot{r}_v/\dot{r}_{cl})^{0.75}} \tag{1.24}$$

where coefficients C_{B1} and C_{B2} are defined as

$$C_{B1} = \frac{2}{2 + 1.25B^{0.75}} \quad \text{and} \quad C_{B2} = \frac{1.25B^{0.75}}{2 + 1.25B^{0.75}} \tag{1.25}$$

Note that blowing number B is for the classical regression rate $\dot{r}_{cl}$ where there is no entrainment and can be estimated by Eq. 1.4. $\dot{r}_{cl}$ is then calculated as slightly modified Marxman Eq. 1.6.

$$\dot{r}_{cl} = \frac{0.03\mu_g^{0.2}}{\rho_f}(1 + \dot{q}_r/\dot{q}_c)BC_{B1}G^{0.8}z^{-0.2} \tag{1.26}$$

All the above equations form a nonlinear set of algebraic equations which can be solved for a given propellant combination to obtain the total regression rate as a function of the axial location and local mass flux. To simplify the nonlinear equations, it is convenient to introduce non-dimensional regression rate variables, where regression rates are normalized by classical regression rate.

$$\phi = \dot{r}/\dot{r}_{cl} \quad , \quad \phi_v = \dot{r}_v/\dot{r}_{cl} \quad , \quad \phi_{ent} = \dot{r}_{ent}/\dot{r}_{cl}$$

and

$$R_{ent} = a_{ent}\frac{G^3}{\dot{r}_{cl}^3} \tag{1.27}$$

Eqs. 1.9, 1.19 and 1.22 can be rewritten into set of three nonlinear equations for the three unknown non-dimensional regression rates. Entrainment parameter R_{ent} is derived from Eq. 1.28 of ϕ_{ent}.

$$\phi_{ent} = \frac{a_{ent}G^3}{\dot{r}^2\dot{r}_{cl}}\frac{\dot{r}_{cl}^2}{\dot{r}_{cl}^2} = \frac{R_{ent}}{\phi^2} \tag{1.28}$$

$$\phi_v + \left(R_{he} + R_{hv}\frac{\phi_v}{\phi}\right)\phi_{ent} = \frac{1}{C_{B1} + C_{B2}\phi_v} \tag{1.29}$$

$$\phi = \phi_v + \phi_{ent} \tag{1.30}$$

From the set of nonlinear equations were numerically evaluated non-dimensional regression rates variables for range of R_{ent} from 0 to 300, which is a practical range of operation, and they are shown in Figure 1.7. Following vales were used in calculation: $B = 4.7$, $R_{he} = 0.051$, $R_{hv} = 0.433$. Then by interpolation was determined simple equation [6]

$$\phi = 1 + 0.61R_{ent}^{0.4} \tag{1.31}$$

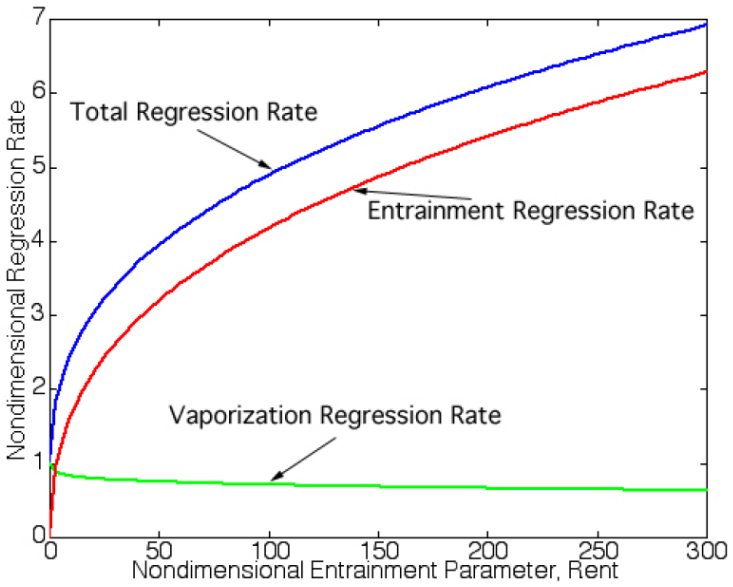

Figure 1.7: Non-dimensional regression rates ϕ as function of entrainment parameter R_{ent} [6]

By combining Eqs. 1.26 and 1.27 is expressed entrainment parameter and for better fit to experimental data exponents are slightly changed [6]

$$R_{ent} = K \frac{a_t^2 \rho_f^2 \rho_l}{\mu_l} C_{B1}^{-2} B^{-3} (1 + \dot{q}_r/\dot{q}_c)^{-3} G^{0.4} z^{0.4} \tag{1.32}$$

Total regression rate can be then simply calculated as

$$\dot{r} = \phi \dot{r}_{cl} \tag{1.33}$$

1.3 Numerical methods

Internal ballistic parameters of combustion chamber can be investigated also using computational fluid dynamic (CFD) modelling, that has been considerably developed recently. CFD modelling is becoming a key tool for reducing the hybrid rocket operation uncertainties and development cost. Using CFD modelling can be predicted the fuel regression rate. It is more advanced than classical analysis that relies only on boundary-layer assumptions to determine the heat flux to the fuel surface. In CFD are also accounted more complex physical interactions, like the effects of turbulence, chemistry, fluid-surface interaction, and radiation. Most of the effort has been addressed to classical non-liquefying fuels. [5] In this theory focus is more on paraffin-based fuels, so the model for polymer fuels is modified to account for the burning of paraffin fuels by including an additional equation for the calculation of the regression rate component determined by the entrainment of liquid fuel into the main flow. [13] The computational approach is able to compute the correct flow field, capture the fluid–surface interaction without losing predictive capabilities, and account for the radiative heat transfer. [14]

A common strategy is solving the Reynolds averaged Navier-Stokes (RANS) equations, with suitable turbulence closure and combustion models. Since chemical and fluid-dynamic characteristic times are much shorter than the regression rate time

scale, steady-state solution of RANS equations is mostly used. [13] In supercritical condition, which is typical for paraffin, viscosity and diffusivity are close to those of a gas and the turbulent diffusion and convection are significantly faster than in the liquid phase, therefore the RANS equations for single-phase multi component turbulent reacting flows can be solved at supercritical turbulent conditions, where fuel is supposed to enter the combustion chamber from the solid wall as 100% gaseous ethylene. Entrainment of fuel in supercritical condition is in form of turbulent mixing process.

Chapter 2

Preliminary motor design

In this chapter is described design process of hybrid rocket engine for specified requirements. Primary use of designed hybrid motor will be in single stage sounding rocket that will be able to reach upper parts of the atmosphere.

2.1 Propellants selection

For the first analytical approach to obtain preliminary design parameters of the motor, Eq. 1.6 for regression rate can be empirically simplified as [8]

$$\dot{r} = a(G_o)^n \tag{2.1}$$

where a and n are regression rate ballistic coefficients that are based on correlations from previous experiments. Units of oxidizer flux G_o are in $[g/cm^2/s]$ ($1\,g/cm^2/s = 10\,kg/m^2/s$) and regression rate $\dot{r}$ in $[mm/s]$. Disadvantage of using this empirical equation is, that ballistic coefficients are determined only for specific combination of fuel and oxidizer and for another fuel with even slightly different properties, ballistic coefficients might be different. Note that also test values of oxidizer flux G_o and regression rate $\dot{r}$ are actually average values of the test burn and not instantaneous values, since it's not possible to measure instantaneous port radius during the burn. For preliminary design and selection of right propellants it is enough and instantaneous values are assumed to be the same as average ones.

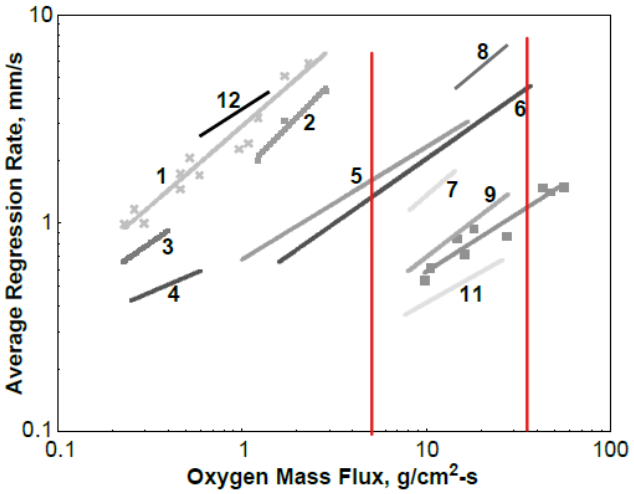

Figure 2.1: Empirical correlations for selected fuels [1]

In Figure 2.1 are shown acquired regression rates correlations for some typical hybrid motor fuels in combination with liquid oxygen. Between red lines is shown range of oxidizer mass fluxes from 5 to 45 $g/cm^2/s$ for designed motor, which will be shown later. For selection of fuel it is important to have the highest possible regression rate at similar operating condition, as for the same size, more thrust can be produced. Highest regression rate has number 8, which is 87% FR5560 Paraffin + 13% nano-sized aluminium, but it's been tested only on short range. Its ballistic coefficients are $a = 0.6$, $n = 0.73$. [1] Number 5 is vortex HTPB, which is not considered, as for simplicity is considered only classical design. Number 6 is FR5560 Paraffin wax (SP-1a) used by Karabeyoglu in his experiments. Its ballistic coefficients are $a = 0.488$, $n = 0.62$. [9] Classical HTPB is number 9, which ballistic coefficients are $a = 0.14$, $n = 0.68$.

As fuel is selected paraffin wax, because it has the highest regression rate for required range of fluxes and is more suitable with its properties. Also its price is relatively low compared to HTPB. As oxidizer, liquid or gaseous oxygen is selected, because of its high oxidizing potential and it's easy to obtain.

For better view, regression rate is plotted as function of oxidizer flux G_o for paraffin wax SP-1a/LOX and HTPB/LOX for comparison, which is shown in Figure 2.2.

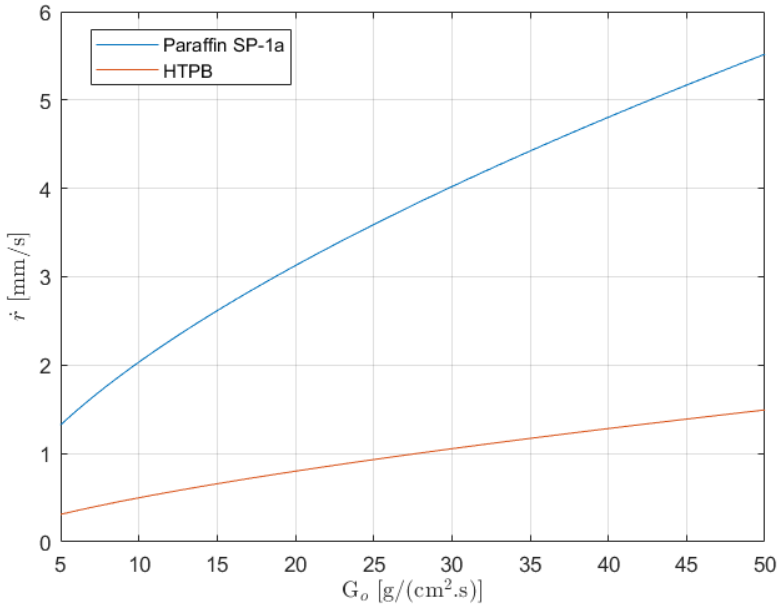

Figure 2.2: Regression rate $\dot{r}(G_o)$ for paraffin SP-1a/LOX and HTPB/LOX

2.1.1 Paraffin FR5560 (SP-1a) properties

As seen in Liquid layer combustion theory by Karabeyoglu, the most crucial parameters of fuel are its viscosity μ_l and density ρ_l at the effective liquid layer temperature. Next important parameters for simulation are its melting and surface temperature. Its number averaged carbon number n is 32 and weight averaged number n_w is 35.2. Ambient temperature T_a is assumed to be 298 K. Melting temperature T_m is calculated based on ABC (asymptotic behavior correlations) method, that can

be used on other alkanes, using equation

$$T_m = Y_\infty - (Y_\infty - Y_0)exp[-\beta(n - n_0)^\gamma] \tag{2.2}$$

where $Y_\infty = 418.07$, $Y_0 = -6288460$, $\beta = 8.929364$, $\gamma = 0.0690406$, $n_0 = 0.34979$. Which for $n = 32$ is 342.9 K (69.75 °C). The most complicated is the surface temperature T_s, which is already calculated by Karabeyoglu and is read from the graph in Figure 2.3 for certain n-alkane. For carbon number $n = 32$ it is about 857 K. Effective fluid layer temperature is then calculated as

$$T_l = \frac{Ts + 2Tm}{3} \tag{2.3}$$

because surface temperature T_s is calculated before droplets entrainment, so after it will be lower. Effective fluid layer temperature T_l is then is 514.3 K.

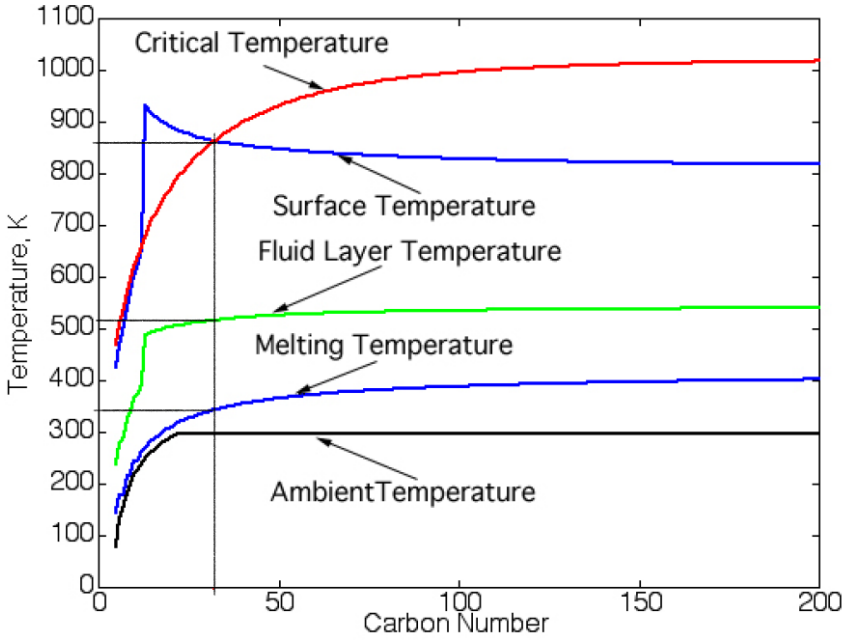

Figure 2.3: The temperature field of n-alkanes[6]

Viscosity and density at liquid phase at the effective fluid temperature are also calculated by ABC method and are plotted in Figure 2.4. Only liquid viscosity μ_l is calculated using weight averaged number. For Paraffin FR5560 it is 0.9 $mPa.s$. Liquid density ρ_l is 674 kg/m^3. Solid fuel density ρ_f is then found to be 920 kg/m^3. [9]

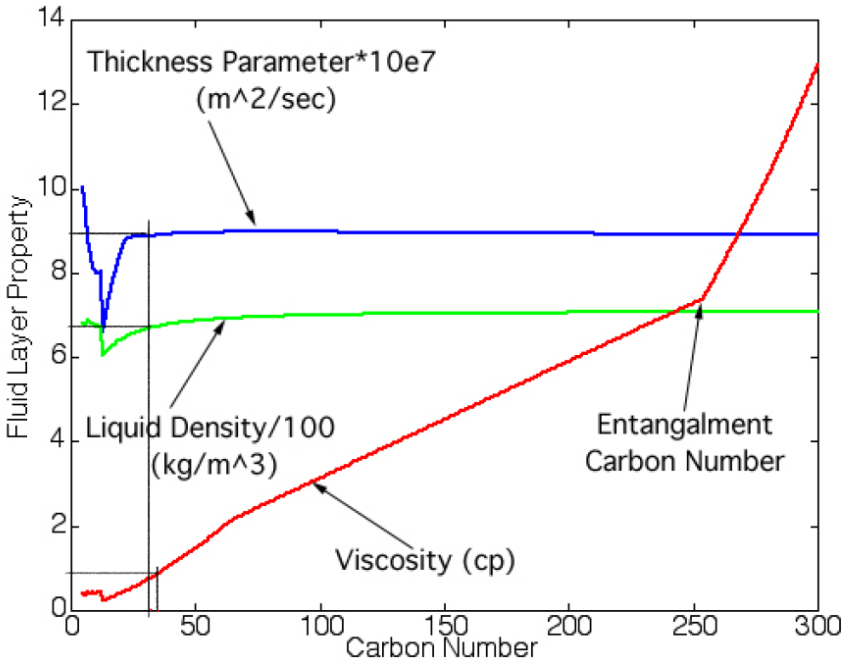

Figure 2.4: The viscosity, liquid density and thickness parameters evaluated at the effective fluid temperature for the series of n-alkanes [6]

2.2 Experimental test results

Test results from already built hybrid motors are very beneficial for design of future motors. Because of the problem with scaling of motors, tests should be taken on motors with similar size. One of them was built in Stanford University and tested at Hybrid Combustion Facility (HCF) at NASA Ames Research Center where its outer diameter is 19.1 cm and grain length L_f 1.15 m and 0.78 m. [9] In table 2.1 are showed results from some selected tests.

R_i $[cm]$	L_f $[m]$	$\dot{m}_o$ $[kg/s]$	G_{o_i} $[g/cm^2/s]$	$\bar{G}_o$ $[g/cm^2/s]$	$\bar{\dot{r}}$ $[mm/s]$	O/F	η_{c^*} [-]	t_b $[s]$
5.6	0.775	2.03	20.60	14.47	2.40	3.05	0.85	9.35
5.65	1.148	2.11	21.04	14.69	2.74	1.78	0.78	8.15
7.05	1.148	4.45	28.50	22.05	3.18	2.69	0.84	6.2
5.85	1.148	4.42	41.11	26.96	3.82	2.48	0.87	7.25
5.65	1.148	4.40	43.87	27.05	3.66	2.57	0.88	8.45
5.65	0.775	4.39	43.77	27.13	3.90	3.84	0.90	8.3
5	1.148	4.43	56.40	32.44	3.84	2.72	0.85	8.25
5.65	1.148	5.55	55.34	34.66	4.25	2.89	0.88	8.2
4.45	1.148	4.44	71.37	36.80	4.17	2.66	0.85	8.3

Table 2.1: Experimental motor tests [9]

From test results can be seen, that c^* efficiency η_{c^*}, which is actual c^* to theoretical, is between 0.78 and 0.9 and it improves with increasing O/F. Maximum theoretical specific impulse is at an O/F ratio of 2.7, but taking into account efficiency, best average O/F ratio is about 3 as can be seen in Figure 2.5. t_b is a burn time of the motor, that depends on initial radius R_i and average regression rate $\bar{\dot{r}}$.

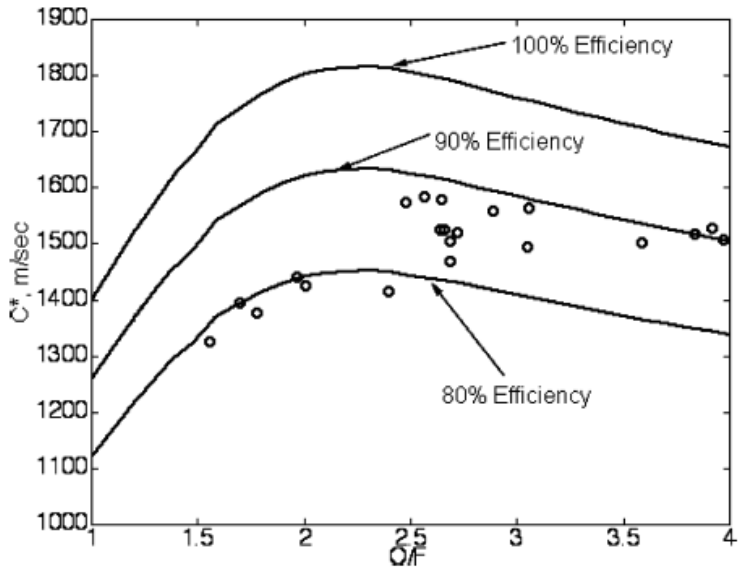

Figure 2.5: Motor delivered c^* as function of O/F [9]

2.3 Combustion chamber design

As the thrust tends to decrease during the burn, initial thrust F_i is therefore assumed to be 15 kN. Initial oxidizer to fuel mass flow rate ratio O/F_i is chosen from Table 1.1 to be 2.5. Into account is also taken that hybrid motors are not 100 % efficient, so it is assumed 90 % efficiency, so then assumed specific impulse is specific impulse from Table 1.1 multiplied by efficiency which is $2\,480.94\,m/s$. Since combustion doesn't depend strongly on pressure, chamber pressure p_c can be then slightly lower than in Table 1.1. Initial chamber pressure is then assumed to be 2.5 MPa. Required initial propellants mass flow rate can be calculated as initial required thrust F_i over specific impulse I_{sp}.

$$\dot{m}_{p_i} = \frac{F_i}{I_{sp}} = \dot{m}_o + \dot{m}_{f_i} \tag{2.4}$$

which is 6.05 kg/s for required thrust. Specific impulse may also slightly vary, depending on the shape of the nozzle, ambient pressure and efficiency of combustion of propellants. Fuel and oxidizer flow rates can be calculated as

$$\dot{m}_{f_i} = \frac{\dot{m}_{p_i}}{O/F_i + 1} \tag{2.5}$$

$$\dot{m}_o = \dot{m}_{p_i} - \dot{m}_{f_i} \tag{2.6}$$

which are 1.73 kg/s and 4.32 kg/s respectively. Oxidizer flow rate is considered to be kept constant during the burn.

Since paraffin wax has relatively high regression rate, fuel grain is then selected as simple single port with cylindrical shape with port radius R. From Eq. 2.1 can be by integrating and some adjustments obtained expression for instantaneous port radius at certain time of the burn [8]

$$R(t) = \left[a(2n+1) \left(\frac{\dot{m}_o}{\pi} \right)^n t + R_i^{2n+1} \right]^{1/(2n+1)} \tag{2.7}$$

where R_i is an initial port radius. Then, by knowing constant oxidizer mass flow rate, oxidizer mass flux based on time $G_o(t)$ can be found and then by using Eq. 2.1 also time progress of regression rate $\dot{r}(t)$ during the burn. Length of the fuel grain can be calculated from relation of initial fuel mass flow rate and burning area as

$$L_f = \frac{\dot{m}_{f_i}}{2\pi R_i \rho_f \dot{r}_i} \tag{2.8}$$

Instantaneous fuel mass flow rate can be then expressed as

$$\dot{m}_f(t) = 2\pi\rho_f L_f a \left(\frac{\dot{m}_o}{\pi}\right)^n \left[a(2n+1)\left(\frac{\dot{m}_o}{\pi}\right)^n t + R_i^{2n+1}\right]^{(1-2n)/(1+2n)} \tag{2.9}$$

In Eq. 2.9 can be seen, that for $n = 0.5$, fuel mass flow rate stays constant during whole burn time, for $n > 0.5$ mass flow rate starts to decrease with time and for $n < 0.5$ it will increase with time. With the same analogy will progress also thrust during the burn, which is dependent on fuel mass flow rate. Typical values of n for classical hybrid motors are between 0.4 and 0.7. So for most cases, fuel mass flow rate decreases with time. With decreasing fuel mass flow rate, O/F ratio starts to increase, which will decrease motor efficiency. Total consumed fuel during burn the whole burn can be expressed as

$$m_f(t_b) = \pi\rho_f L_f \left[a(2n+1)\left(\frac{\dot{m}_o}{\pi}\right)^n t_b + R_i^{2n+1}\right]^{(1-2n)/(1+2n)} \tag{2.10}$$

Since length of the fuel grain depends on initial radius, it's good to analyze, how change of R_i will affect other motor properties. Firstly is analyzed final radius R_f. Using Eq. 2.7, final radii are then calculated for set of initial radii and also for different burn times t_b. Secondly are calculated lengths of fuel grain, where initial fuel mass flow rate is selected by required thrust. With increasing initial radius is also increasing required fuel grain length. Also using Eq. 2.10 is calculated consumed fuel mass for different R_i and t_b. With increasing burn time is also increasing final radius, and therefore also required propellants mass. Then initial thrust to weight ratio TWR is decreasing with increasing burn time. It can be seen from analysis that the smaller the initial radius, the slightly higher the TWR. Initial radius is then limited only by "flooding" limit, therefore the highest possible initial regression rate that will be in normal regime. Final radius is then limited by lowest possible regression rate and also required lowest TWR for the rocket to be able to lift off, which is defined by the burn time. Burn time t_b is then analysed and estimated in next subsection. "Flooding" limit of the maximum oxidizer flux is set by the range of fluxes from already conducted tests on paraffin wax. Maximum initial oxidizer flux of successful test was about 70 $g/cm^2/s$. [9] Initial radius can be calculated as

$$R_i = \sqrt{\frac{\dot{m}_o}{\pi G_{o_i}}} \tag{2.11}$$

Therefore for oxidizer mass flow rate 4.32 kg/s, minimum initial port radius is 4.43 cm. Although most of the other tests had lower initial oxidizer mass flux, so then initial port radius is selected to be 5.5 cm with initial oxidizer mass flux of 45.5 $g/cm^2/s$ and initial regression rate about 5.2 mm/s.

2.3.1 Burn time analysis

In this section are analysed motor properties that depend on selected burn time of the motor. Analysis is using values from Table 2.3 and is done for burn times 30 s, 45 s and 60 s. Properties that are affected by burn time are final (outer) radius R_f, propellants mass m_p, dry mass m_d (construction), thrust to weight ratio of the whole rocket and the height that the rocket will reach.

Final radius is calculated using Eq. 2.7, oxidizer mass is calculated as $m_o = \dot{m}_o t_b$ and fuel mass using Eq. 2.10. Dry mass is assumed to be 70 % of propellants mass. This assumption is very general and might later change by analyzing structure more deeply. Thrust F is then calculated for small time intervals $\Delta t = 0.1\ s$ by multiplying specific impulse I_{sp} by propellants mass flow rate $\dot{m}_p = \dot{m}_o + \dot{m}_f$, where fuel mass flow rate is calculated using Eq. 2.9. Instantaneous rocket mass is calculated as reversed vector of calculated propellants masses for each time interval plus dry mass. Then can be calculated instantaneous thrust to weight ratios during the burn.

To calculate the height that the rocket will reach when starting vertically, drag force also has to be taken into account. Drag force can be calculated as

$$F_{D_n} = \frac{1}{2}\rho_n {v_n}^2 C_D A \tag{2.12}$$

where ρ_n is air density at certain height h_n using standard atmosphere, C_D is drag coefficient which is for the conical tip 0.5 and A is cross section area, where radius is taken as final radius for certain burn time plus thickness that is assumed as 3 cm. Acceleration is then calculated by small time intervals as

$$a_n = \frac{F_n - F_{D_n} - m_{tot_n} g}{m_{tot_n}} \tag{2.13}$$

where $n = 0, 1, 2, ...$ Velocity and height are then calculated by small time intervals until burn time is reached as

$$v_{n+1} = v_n + a_n \Delta t \tag{2.14}$$

$$h_{n+1} = h_n + v_n \Delta t \tag{2.15}$$

their final values are then burnout velocity v_{out} and height h_{out}. After burnout rocket continues to climb up and starts to decelerate due to gravity and drag force until maximum height h_{max} where it reaches zero velocity. In Table 2.2 are calculated values for three different burn times. Since there is not great difference in maximum reached heights between 45 s and 60 s, therefore burn time t_b of around 45 s seems to be the best option, so final radius R_f is then rounded to 16 *cm* and burn time is then around 48 s.

t_b [s]	30	45	60
R_f [cm]	13.24	15.51	17.43
m_p [kg]	174.17	259.1	343.28
m_d [kg]	121.92	181.35	240.3
TWR_i [-]	5.16	3.47	2.62
v_{out} [m/s]	1230	1251	1217
h_{out} [km]	17.43	24.37	29.91
h_{max} [km]	76.26	97.61	102.8

Table 2.2: Burn time analysis

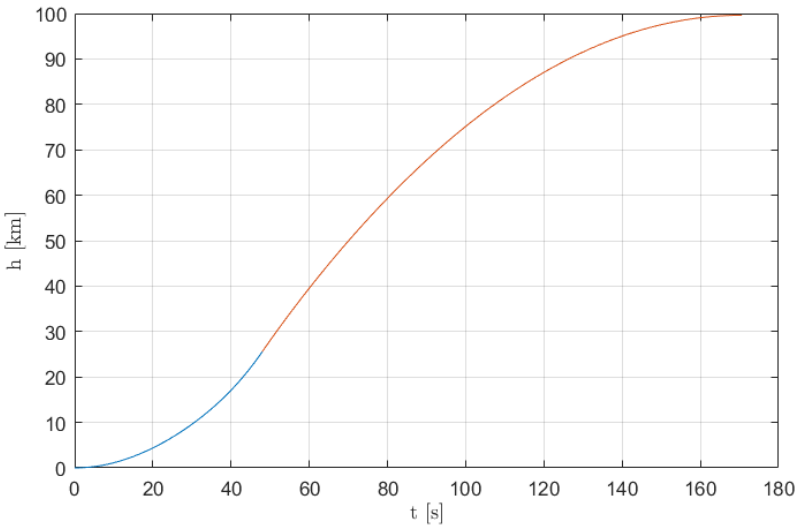

Figure 2.6: Height profile of rocket flight with t_b=48 s

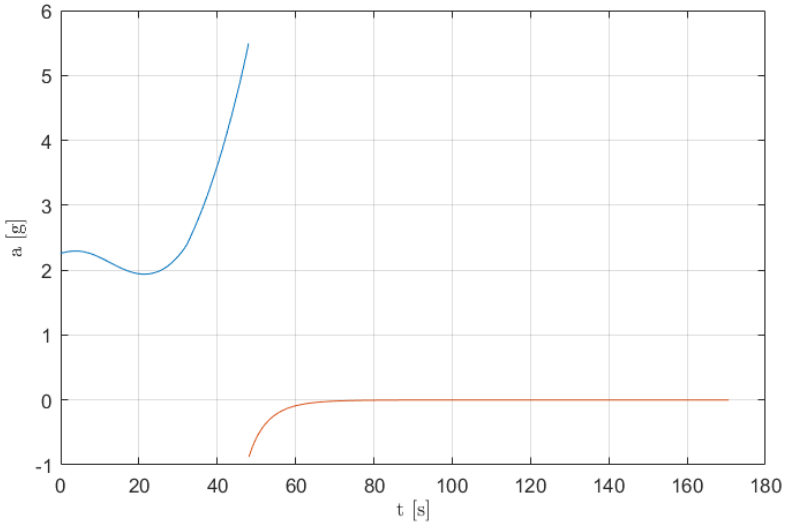

Figure 2.7: Acceleration profile of rocket flight with t_b=48 s

In Figure 2.6 can be seen height profile of rocket flight, where height in blue is during motor burn and in orange is after motor burn when rocket is decelerating. Maximum reached height is 99.6 km. From Figure 2.7 can be seen, that maximum reached acceleration is at the end of the burn and is 5.5 g. The largest uncertainty that might affect the results is rocket empty mass which consists of motor construction as combustion chamber, oxidizer tank, piping, valves, injector, nozzle, rocket structure and payload. The second largest uncertainty is actual specific impulse and therefore also actual thrust. As the oxidizer to fuel ratio increases during the burn, specific impulse will tend decrease. On the other hand with increasing height, ambient pressure will decrease, therefore specific impulse will increase.

2.3.2 Preliminary results

Eq. 2.1 is valid only for oxidizer to fuel ratios between 1.7 and 2.3. For O/F ratios significantly higher it is better to use following equation with O/F correction [9]

$$\dot{r} = \frac{0.163 G_o^{0.62}}{\left[(1 + \frac{1}{O/F})^{0.38} - 1\right] O/F} \tag{2.16}$$

Firstly by using Eq. 2.1 at the beginning of the burn, O/F is 2.5 which is relatively close and doesn't need to be corrected, but at the end of the burn is 3.3 which is getting more significantly higher and then equation with O/F correction should be used. All results in Tables 2.2 and 2.3 are then calculated using equation with O/F correction, where port radius is calculated at small time steps with $\Delta t = 0.1\,s$.

In Table 2.3 are summarised selected and calculated values for preliminary design of hybrid motor using paraffin wax SP-1a and liquid oxygen as propellants. Note that this design is only based on equation that was evaluated from calculated average regression rates for average oxidizer mass flux. Therefore in next chapter is done more detailed analysis and simulation.

Initial thrust	F_i	15 000 N
Average thrust	$\bar{F}$	14 264 N
Initial oxidizer to fuel ratio	$\mathrm{O/F}_i$	2.5
Final oxidizer to fuel ratio	$\mathrm{O/F}_f$	3.3
Specific impulse	I_{sp}	2 480.94 $N.s/kg$
Initial port radius	R_i	5.5 cm
Final port radius	R_f	16 cm
Burn time	t_b	48 s
Solid fuel density	ρ_f	920 kg/m^3
Average regression rate	$\bar{\dot{r}}$	2.17 mm/s
Oxidizer mass flow rate	$\dot{m}_o$	4.32 kg/s
Initial propellants mass flow rate	$\dot{m}_{p_i}$	6.05 kg/s
Average propellants mass flow rate	$\bar{\dot{m}}_p$	5.75 kg/s
Oxidizer mass	m_o	207.3 kg
Fuel mass	m_f	69.2 kg
Fuel grain length	L_f	1.06 m
Initial chamber pressure	p_c	2.5 MPa

Table 2.3: Initial design parameters for Paraffin/LOX propellant combination

Average values were calculated as arithmetic average from all values during the burn. Average regression rate $\bar{\dot{r}}$ is also the same as difference between initial and final port radius divided by the burn time. Oxidizer mass was calculated by multiplying oxidizer mass flow rate by the burn time. Fuel mass was calculated as volume of fuel grain times fuel density.

In following figures are shown predicted combustion chamber parameters as regression rate $\dot{r}$, port radius R, thrust F and oxidizer to fuel ratio O/F during the burn for preliminary design. Decreasing thrust is caused by decreasing fuel mass flow rate during the burn.

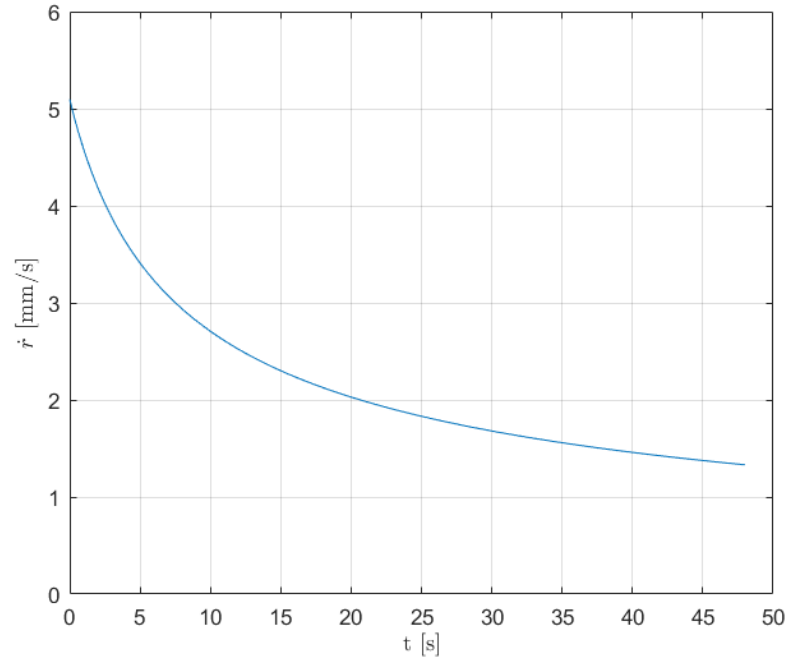

Figure 2.8: Regression rate $\dot{r}$ of preliminary design during burn time

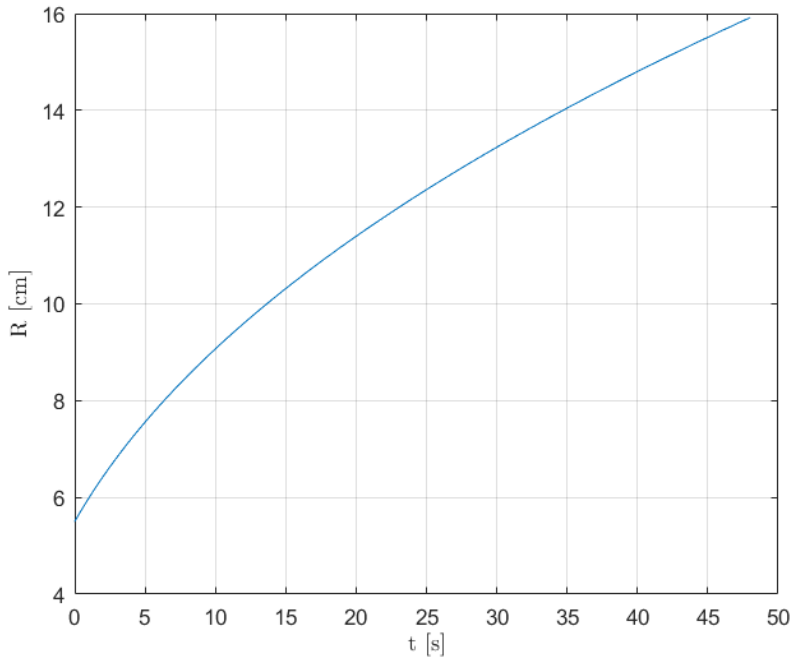

Figure 2.9: Port radius R of preliminary design during burn time

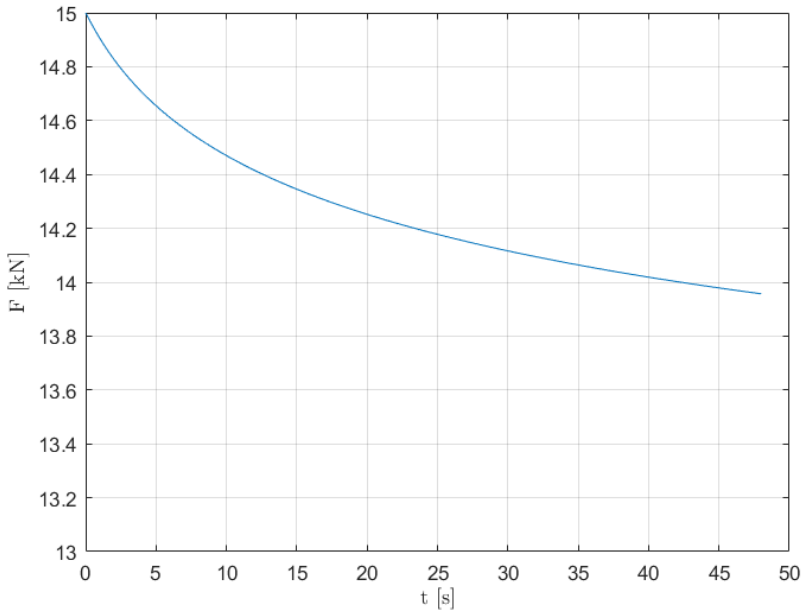

Figure 2.10: Thrust F of preliminary design during burn time (constant $I_{sp} = 2481\,m/s$)

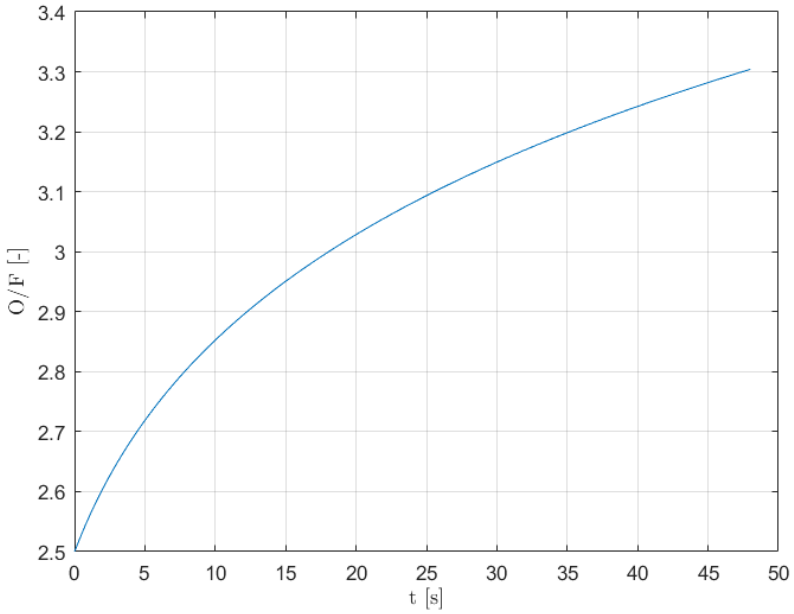

Figure 2.11: Oxidizer to fuel ratio O/F of preliminary design during burn time

2.4 Motor performance

From previous experiments can be estimated characteristic velocity c^* that is from Figure 2.5 assumed to be 1550 m/s and constant during the burn since efficiency is improving and ideal c^* is decreasing with increasing O/F ratio. Characteristic velocity can be expressed as

$$c^* = \frac{p_c A_t}{\dot{m}_p} \tag{2.17}$$

and when chamber pressure p_c is chosen to be 2.5 MPa and initial propellants mass flow rate $\dot{m}_{p_i}$ is 6.05 kg/s, then calculated throat area A_t is 38.236 cm^2, then throat diameter can be calculated as $D_t = 2\sqrt{A_t/\pi} = 6.98\ cm$. As the propellants mass flow rate will decrease during the burn, chamber pressure is also expected to decrease.

In order to obtain theoretical internal properties resulted from the combustion process, NASA CEA (Chemical Equilibrium with Applications) [15] online software is used. Calculated parameters are theoretical at equilibrium point of reaction, so actual values might slightly differ. Following theoretical parameters of exhaust gas are chamber temperature T_c, density of gas ρ_g, average molar mass $\bar{M}$, specific heat capacity at constant pressure c_p and ratio of specific heats γ and they are found for O/F range from 2.5 to 3.3 and γ and $\bar{M}$ are plotted in Figures 2.12 and 2.13. In Figures 2.15, 2.16 and 2.17 are shown all parameters at initial, average and final O/F 2.5, 3 and 3.3.

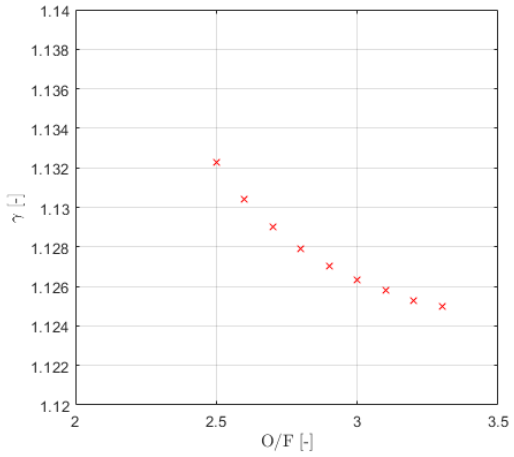

Figure 2.12: γ(O/F)

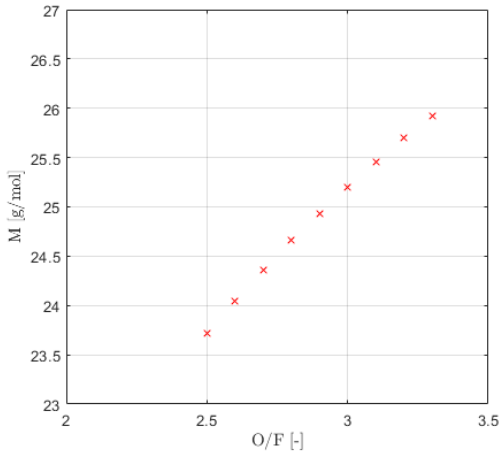

Figure 2.13: $\bar{M}$(O/F)

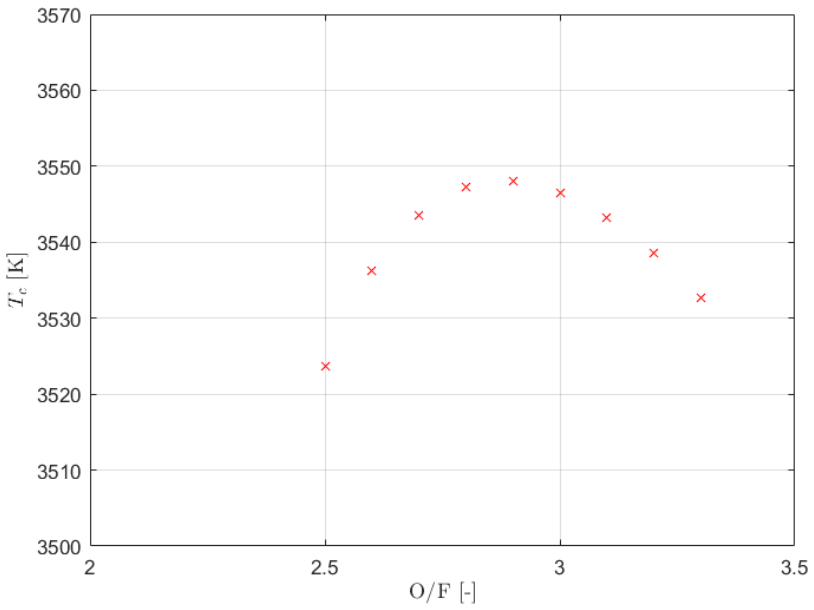

Figure 2.14: Chamber temperature T_c as function of O/F

```
Pin =   362.6 PSIA
CASE = Paraffin_______

            REACTANT                    WT FRACTION      ENERGY      TEMP
                                         (SEE NOTE)     KJ/KG-MOL      K
FUEL        paraffin                     1.0000000  -1860600.000    298.000
OXIDANT     O2(L)                        1.0000000    -12979.000     90.170

O/F=    2.50000  %FUEL= 28.571429  R,EQ.RATIO= 1.328804  PHI,EQ.RATIO= 1.328804

                CHAMBER   THROAT
Pinf/P            1.0000   1.7277
P, BAR            25.000   14.470
T, K             3523.70  3356.87
RHO, KG/CU M    2.0237 0 1.2476 0
H, KJ/KG         -820.38 -1474.95
U, KJ/KG        -2055.77 -2634.81
G, KJ/KG        -40907.1 -39663.8
S, KJ/(KG)(K)    11.3763  11.3763

M, (1/n)          23.716   24.064
(dLV/dLP)t      -1.04567 -1.04014
(dLV/dLT)p        1.8136   1.7530
Cp, KJ/(KG)(K)    7.0965   6.8870
GAMMAs            1.1323   1.1287
SON VEL,M/SEC     1182.7   1144.2
MACH NUMBER        0.000    1.000
```

Figure 2.15: Theoretical combustion chamber parameters at O/F=2.5 [15]

```
Pin =   362.6 PSIA
CASE = Parafin________

            REACTANT                    WT FRACTION      ENERGY      TEMP
                                         (SEE NOTE)     KJ/KG-MOL      K
FUEL        paraffin                     1.0000000  -1860600.000    298.000
OXIDANT     O2(L)                        1.0000000    -12979.000     90.170

O/F=    3.00000  %FUEL= 25.000000  R,EQ.RATIO= 1.107337  PHI,EQ.RATIO= 1.107337

                CHAMBER   THROAT
Pinf/P            1.0000   1.7234
P, BAR            25.000   14.506
T, K             3546.52  3391.37
RHO, KG/CU M    2.1366 0 1.3165 0
H, KJ/KG         -768.54 -1386.56
U, KJ/KG        -1938.64 -2488.47
G, KJ/KG        -39585.6 -38505.5
S, KJ/(KG)(K)    10.9451  10.9451

M, (1/n)          25.201   25.590
(dLV/dLP)t      -1.05792 -1.05444
(dLV/dLT)p        2.0326   2.0182
Cp, KJ/(KG)(K)    8.0135   8.1206
GAMMAs            1.1263   1.1217
SON VEL,M/SEC     1148.0   1111.8
MACH NUMBER        0.000    1.000
```

Figure 2.16: Theoretical combustion chamber parameters at O/F=3 [15]

REACTANT		WT FRACTION (SEE NOTE)	ENERGY KJ/KG-MOL	TEMP K
FUEL	paraffin	1.0000000	-1860600.000	298.000
OXIDANT	O2(L)	1.0000000	-12979.000	90.170

O/F= 3.30000 %FUEL= 23.255814 R,EQ.RATIO= 1.006670 PHI,EQ.RATIO= 1.006670

	CHAMBER	THROAT
Pinf/P	1.0000	1.7225
P, BAR	25.000	14.513
T, K	3532.63	3380.10
RHO, KG/CU M	2.2067 0	1.3595 0
H, KJ/KG	-743.22	-1341.25
U, KJ/KG	-1876.11	-2408.80
G, KJ/KG	-38620.3	-37582.9
S, KJ/(KG)(K)	10.7221	10.7221
M, (1/n)	25.927	26.325
(dLV/dLP)t	-1.05862	-1.05540
(dLV/dLT)p	2.0527	2.0430
Cp, KJ/(KG)(K)	7.9622	8.0950
GAMMAs	1.1250	1.1204
SON VEL,M/SEC	1128.9	1093.6
MACH NUMBER	0.000	1.000

Figure 2.17: Theoretical combustion chamber parameters at O/F=3.3 [15]

2.4.1 Specific impulse and nozzle

After knowing theoretical parameters of exhaust gas, actual specific impulse I_{sp} can be calculated as

$$I_{sp} = C_F c^* \tag{2.18}$$

where C_F is thrust coefficient, that reflects the expansion properties of the exhaust gas and it gives the amplification of the thrust due to the gas expansion in the supersonic nozzle compared to the thrust delivered if the chamber pressure only acted over the throat area. Nozzle starts at the throat area A_t, where hot gases are at speed of sound, then it's increasing where hot gases expand. Its shape can be either simple cone with 15° or 20° angle or it can be in shape of bell, with special geometry, that optimizes performance of the nozzle. Shape of the nozzle will be chosen in future work. C_F can be expressed as

$$C_F = \gamma \sqrt{\frac{2}{\gamma - 1}\left(\frac{2}{\gamma + 1}\right)^{\frac{\gamma+1}{\gamma-1}}\left[1 - \left(\frac{p_e}{p_c}\right)^{\frac{\gamma-1}{\gamma}}\right]} + \frac{p_e - p_a}{p_c}\epsilon \tag{2.19}$$

where p_e, p_c and p_a are the exit pressure of the nozzle, chamber pressure and ambient pressure respectively and ϵ is ratio of area at the exit to the throat area of the nozzle. Which can be also expressed as

$$\epsilon = \frac{A_e}{A_t} = \left(\frac{\gamma + 1}{2}\right)^{-\frac{\gamma+1}{2(\gamma-1)}} \frac{\left(1 + \frac{\gamma-1}{2}M_e^2\right)^{\frac{\gamma+1}{2(\gamma-1)}}}{M_e} \tag{2.20}$$

M_e is mach number at the exit of the nozzle. Exit pressure p_e can be expressed as

$$p_e = p_c \left(1 + \frac{\gamma - 1}{2}M_e^2\right)^{\frac{\gamma}{\gamma-1}} \tag{2.21}$$

Combining Equations 2.19, 2.20 and 2.21 as a function of M_e can be from the plot determined maximum thrust coefficient at sea level and therefore specific

impulse, where ambient pressure p_a is 1 atm (101 325 Pa), ratio of specific heats γ is assumed to be as at the beginning of the burn, so 1.1323 and combustion chamber pressure p_c is 2.5 MPa. In Figures 2.18 and 2.19 are plotted area ratio ϵ and exit pressure p_e as function of exit mach number. Exit mach number increases with increasing exit nozzle area A_e, but with increasing A_e is decreasing exit pressure of the nozzle. Using Eq. 2.19 to calculate C_F, and then Eq. 2.18 to calculate specific impulse, that is then is plotted in Figure 2.20 for different ambient pressures which are decreasing during flight with increasing altitude. Maximum I_{sp} is when exit pressure is equal to ambient pressure, therefore ideal would be, if nozzle exit area would be continuously increasing.

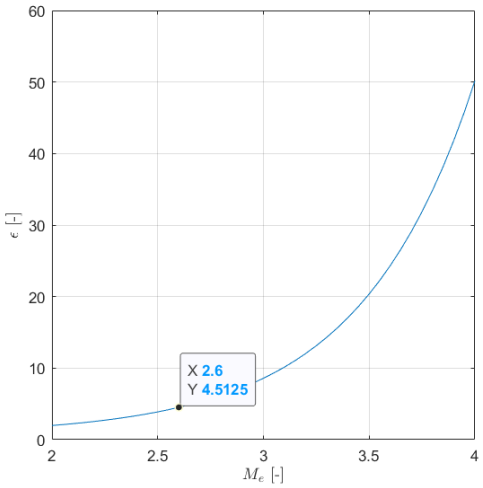

Figure 2.18: $\epsilon(M_e)$

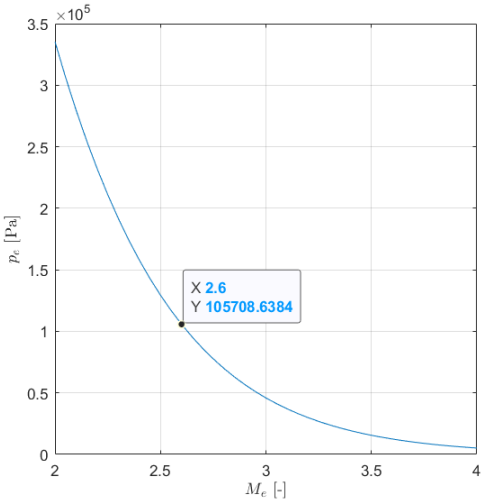

Figure 2.19: $p_e(M_e)$

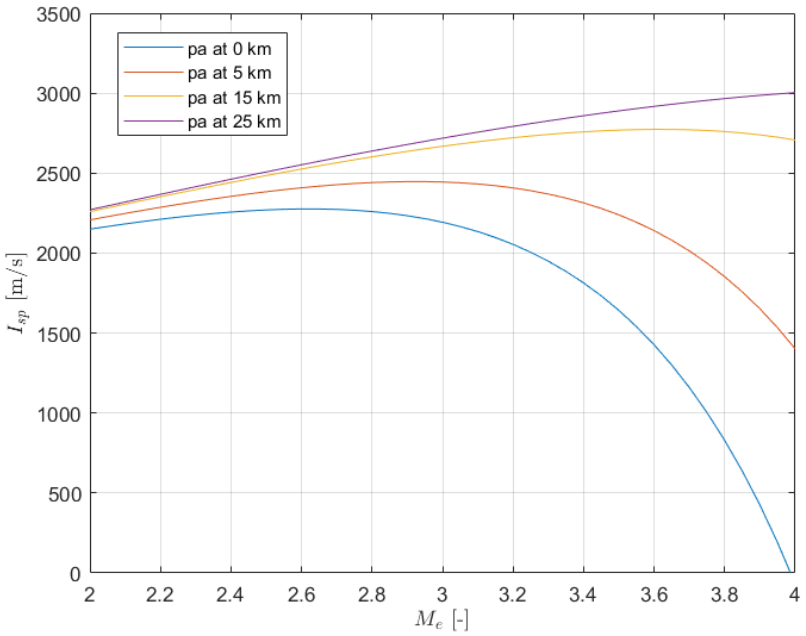

Figure 2.20: $I_{sp}(M_e)$ ($p_c = 2.5\ MPa$, $c^* = 1550\ m/s$)

Area ratio ϵ should be selected in range of M_e between 2.6 when I_{sp} at sea level is maximum and 2.9 when it is still relatively high. Area ratio is then in range between 4.513 and 7.269. In Table 2.4 are shown specific impulses at three selected exit mach numbers 2.6, 2.8 and 2.9 at different altitudes. At sea level, maximum $I_{sp} = 2276\ m/s$, but then with constant A_e it doesn't increase that much at higher altitudes and at altitude of 25 km where is predicted burnout, $I_{sp} = 2552\ m/s$, when at area ratio of 7.269 I_{sp} at 25 km is 2679 m/s. If throat area A_t is 38.236 cm^2, then the area at the exit of the nozzle A_e should be in range between 172.56 and 277.9 cm^2 and the exit diameter of the nozzle D_e between 14.8 and 18.8 cm. Selection of area ratio and design of nozzle will depend on how exactly high thrust is needed during flight, that can be found in simulation of burn or at real firing tests of the motor.

h $[km]$	p_a $[Pa]$	I_{sp} at $\epsilon = 4.513$ $[m/s]$	I_{sp} at $\epsilon = 6.178$ $[m/s]$	I_{sp} at $\epsilon = 7.269$ $[m/s]$
0	101 325	2276	2259	2233
5	54 012	2408	2441	2447
15	12 041	2525	2601	2636
25	2 510	2552	2638	2679

Table 2.4: Specific impulse at different altitudes with different area ratio

Chapter 3

Simulation

Analytical simulation of the burn is done using Karabeyouglu's liquid layer combustion theory.

3.1 Analytical simulation of the burn

Process of simulation is according to Karabeyouglu's liquid layer combustion theory described in section 1.2.2. It is done similarly as in Ref. [16]. In Table 3.1 are summarised properties of Paraffin FR5560. Liquid parameters are at effective liquid temperature $T_l = 514.3\ K$. Firstly is calculated thickness parameter a_t using Eq. 1.17 which is $9.965{\times}10^{-8}\ m^2/s$. Then blowing parameter B was estimated from Figure 3.1 to 4.7 and blowing correction parameter C_{B1} was calculated using Eq. 1.25 to 0.3339. Initial parameters as fuel grain length L_f, initial port radius R_i, oxidizer mass flow rate $\dot{m}_o$ and burn time t_b were chosen from preliminary design in Table 2.3.

λ_l	μ_l	ρ_l	c_l	c_s	L_m	T_m	T_s	h_m
$[W/(m.K)]$	$[mPa.s]$	$[kg/m^3]$	$[J/(kg.K)]$	$[J/(kg.K)]$	$[kJ/kg]$	$[K]$	$[K]$	$[kJ/kg]$
0.135	0.9	674	2725.5	2030	170	342.9	857	261.1

Table 3.1: Paraffin chemical properties

Simulation is done by dividing burn time into time steps with $\Delta t = 0.05$ s, which are represented with index i. Fuel grain length is axially split into 501 nodes (500 elements, each long $\Delta z = 2.12mm$), that are represented with index j. Simulation starts at $t = 0$ s ($i = 1$), where port radius is at each axial location initial port radius. Then local mass flux $G_{i,j}$, which units are in $kg/m^2/s$, is calculated as

$$G_{i,j} = \frac{\dot{m}_o + \sum_{n=2}^{j} \dot{m}_{f_{i,n-1}}}{\pi R_{i,j}} \tag{3.1}$$

At axial location $z = 0$ m ($j = 1$), fuel mass flow rate $\dot{m}_{f_{1,1}}$ is 0 kg/s and local mass flux $G_{1,1} = \dot{m}_o/(\pi R_{1,1})$. At second node ($z = 0.00212$ m), $G_{1,2} = G_{1,1} = 454.58\, kg/m^2/s$. Entrainment parameter R_{ent} can be then calculated using Eq. 1.32. Then using Eqs. 1.26, 1.31 and 1.33 is calculated local regression rate $\dot{r}_{1,2}$ which is equal also to regression rate at firs node $\dot{r}_{1,1}$. At the end, fuel mass flow rate at each next node is calculated as

$$\dot{m}_{f_{1,j}} = \dot{r}_{1,j}/1000\rho_f \Delta z 2\pi R_{1,j} + \dot{m}_{f_{1,j-1}} \tag{3.2}$$

The same process is then done at each next node until the end of the fuel grain. At each next time step are firstly calculated new local port radii as

$$R_{i,j} = R_{i-1,j} + \dot{r}_{i-1,j}\Delta t/1000 \tag{3.3}$$

and then the same process as at first time step is repeated.

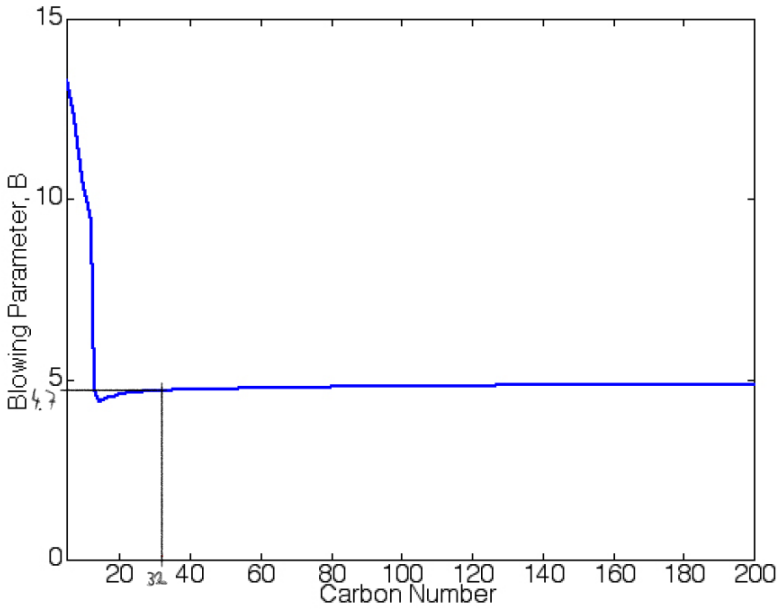

Figure 3.1: Blowing parameter B for series of n-alkanes [6]

To be able to do simulation, entrainment parameter constant K needs to be estimated. It is estimated by matching simulation average results to real experimental test results from Karabeyoglu [9] in Table 2.1, because the tested motor had similar size to the motor that was initially designed in previous chapter. Entrainment parameter constant K was estimated to be 1.6×10^4 to as closely as possible match experimental results.

3.1.1 Results of analytical simulation

In Table 3.2 are summarised initial and average results of thrust (assuming constant $I_{sp} = 2276\ m/s$ calculated in previous chapter), propellants mass flow rate, regression rate, oxidizer mass flux and oxidizer to fuel ratio of the simulation for burn time $t_b = 48\ s$. Propellants mass flow rate is calculated as sum of the constant oxidizer mass flow rate $\dot{m}_o$ which is 4.32 kg/s and fuel mass flow rate at the end of fuel grain. Average regression rate is lower than predicted in preliminary design, therefore final average port radius is smaller than 16 cm and until all fuel get burned, actual burn time will be higher than 48 s.

In the following figures are plotted final results of the analytical simulation. These simulation results should be more precise then the preliminary design. As can be seen in Figure 3.2, on the beginning of the fuel grain, regression rate $\dot{r}$ is very high because of the small axial distance z which results from Eq. 1.26, where if $z = 0$ m, $\dot{r}$ should be infinite, which of course isn't real. Then it drops very fast and at distance about 20 cm it is at minimum and starts slightly increasing towards the end of the grain. This reflects on progress of the port radius R in Figure 3.3, where it reaches 16 cm only at the beginning.

F_i [N]	$\bar{F}$ [N]	$\dot{m}_{p_i}$ [kg/s]	$\bar{m}_p$ [kg/s]	$\bar{\dot{r}}$ [mm/s]	$\bar{G}_o$ [$g/cm^2/s$]	O/F$_i$ [-]	O/F$_f$ [-]	$\bar{O/F}$ [-]
14 730	12 454	6.46	5.46	1.87	13.05	2.02	5.04	3.87

Table 3.2: Results of the analytical simulation

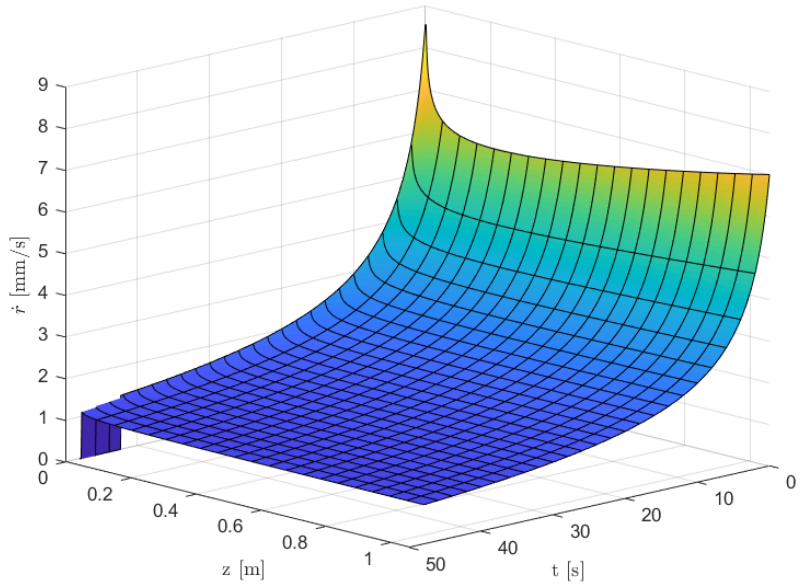

Figure 3.2: 3D plot of regression rate $\dot{r}$ along fuel grain during the burn

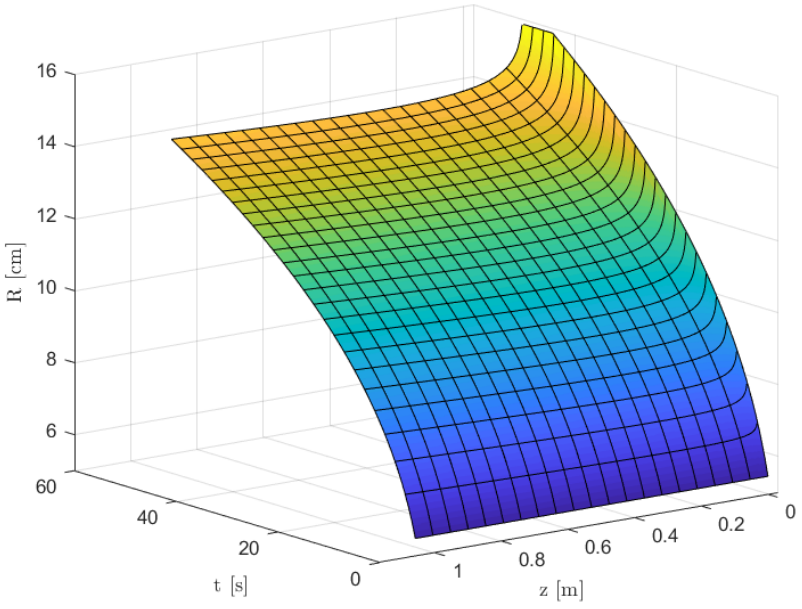

Figure 3.3: 3D plot of port radius R along fuel grain during the burn

Then are calculated average values of regression rate and port radius along the fuel grain and are plotted in Figures 3.4 and 3.5.

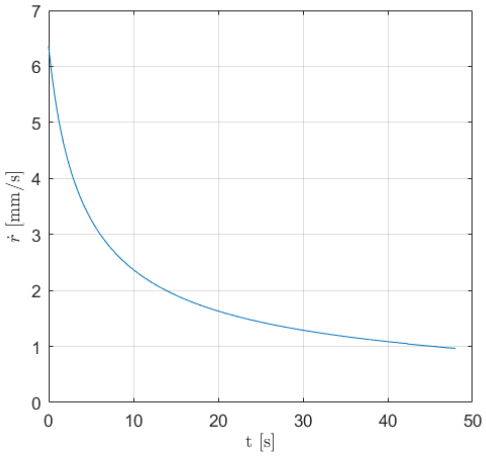

Figure 3.4: $\bar{\dot{r}}(t)$

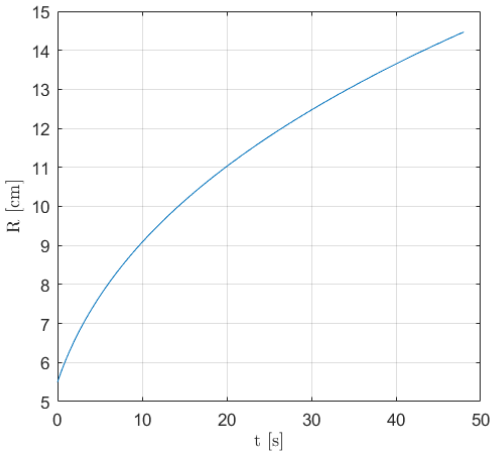

Figure 3.5: $\bar{R}(t)$

Since this simulation was done by matching entrainment parameter constant K to approximate average regression rate and O/F ratio of previous experiments, and done based on analytical theory, actual process of burning might be slightly different, which should be compared in experimental test of the motor. If the simulation is correct, then initial fuel grain radius could be adjusted along the grain, to burn at the same rate.

In Figure 3.6 is plotted predicted thrust for different I_{sp} during flight. Simulated thrust is decreasing more rapidly compared to the thrust of preliminary design, therefore predicted altitude profile during flight might be slightly lower than of preliminary design. Overall thrust can be increased by increasing oxidizer mass flow rate $\dot{m}_o$ and also increasing length of fuel grain to not change the O/F ratio. Another option could be to increase initial burning area by non-circular shape of port.

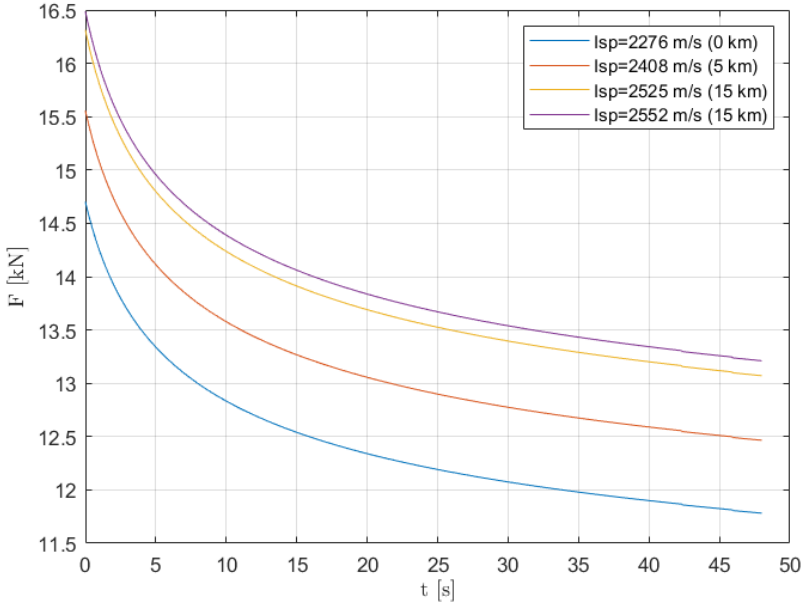

Figure 3.6: Thrust during the burn time for different I_{sp} during flight

Conclusion

Goal of this work was to propose a concept of combustion chamber of hybrid rocket motor with thrust higher than 10 kN, that can be primarily used in sounding rocket into mesosphere. Firstly were discussed existing fuels and oxidizers, from which were chosen paraffin wax as fuel and liquid oxygen (LOX) as oxidizer. Then were discussed existing models of combustion as classical theory of G.A. Marxman, modified theory for liquefying fuels of A. Karabeyoglu and modern numerical CFD model.

Preliminary design of motor was done based on empirical relation for chosen propellants, that is based on past experimental results. Initial required thrust was selected 15 kN and required oxidizer mass flow rate $\dot{m}_o$ was calculated to be 4.32 kg/s. Design of oxidizer inlet system could be designed for slightly higher oxidizer mass flux than nominal of 4.32 kg/s in case of insufficiently high enough trust as predicted. Preferably about 5 kg/s. Fuel grain was designed as a single port with initial port diameter 11 cm and outer diameter 32 cm with length of 1.06 m. Properties of combustion gas as ratio of specific heats, average molar mass and chamber temperature were found using NASA CEA (Chemical Equilibrium with Applications) online software as a function of oxidizer to fuel ratio which increases during the burn. Maximum chamber pressure was selected to be 2.5 MPa. Nozzle throat diameter was calculated to be 6.98 cm and exit diameter between 14.8 and 18.8 cm.

By inserting preliminary design parameters, burn of the motor was simulated based on the analytical liquid layer combustion theory of Karabeyoglu [6]. One uncertainty that might cause different results is the empirical entrainment parameter constant K that can be freely adjusted and was only estimated by matching experimental test results of Karabeyoglu [9]. Average regression rate of simulation was 1.87 mm/s which is slightly lower than predicted by empirical relation for regression rate, that was 2.17 mm/s. Therefore also produced thrust was lower, than selected thrust of 15 kN. To fully validate the results of the simulation, a test motor with given dimensions should be built and experimentally tested. Then the simulation should be compared with experimental data of the measurements.

Future studies could be also focused on non-classical concepts of hybrid rocket motors, as for example vortex motor, or helical fuel grain to increase even more regression rate.

This study together with study of construction of hybrid motor and study of the optimization of the nozzle serve as base guidelines for future more detailed design for building a hybrid rocket motor.

List of Figures

List of Tables

Bibliography

[1] M. J. Chiaverini, "Review of solid-fuel regression rate behavior in classical and nonclassical hybrid rocket motors", in *Fundamentals of hybrid rocket combustion and propulsion*. American Institute of Aeronautics and Astronautics, 2007, pp. 37–125.

[2] Y.-S. Chen, "Development of hapith small launch vehicle based on hybrid rocket propulsion", *AIAA Propulsion and Energy 2019 Forum*, 2019. DOI: 10.2514/6.2019-3837.

[3] K. K. Kuo and M. Chiaverini, "Challenges of hybrid rocket propulsion in the 21st century", in *Fundamentals of hybrid rocket combustion and propulsion*. American Institute of Aeronautics and Astronautics, 2007, pp. 593–638.

[4] D. Altman and A. Holzman, "Overview and history of hybrid rocket propulsion", in *Fundamentals of hybrid rocket combustion and propulsion*. American Institute of Aeronautics and Astronautics, 2007, pp. 1–36.

[5] V. Sankaran, "Computational fluid dynamics modeling of hybrid rocket flowfields", in *Fundamentals of hybrid rocket combustion and propulsion*. American Institute of Aeronautics and Astronautics, 2007, pp. 323–350.

[6] A. Karabeyoglu, B. Cantwell, and J. Stevens, "Evaluation of the homologous series of normal alkanes as hybrid rocket fuels", *41st AIAA/ASME/SAE/ASEE Joint Propulsion Conference amp; Exhibit*, 2005. DOI: 10.2514/6.2005-3908.

[7] C. Carmicino, G. Gallo, and R. Savino, "Self-consistent surface-temperature boundary condition for liquefying-fuel-based hybrid rockets internal-ballistics simulation", *International Journal of Heat and Mass Transfer*, vol. 169, 2021. DOI: 10.1016/j.ijheatmasstransfer.2021.120928.

[8] G. P. Sutton and O. Biblarz, "Hybrid propellant rockets", in *Rocket propulsion elements*. Wiley, 2010.

[9] A. Karabeyoglu, G. Zilliac, B. Cantwell, S. Zilwa, and P. Castelluci, "Scale-up tests of high regression rate liquefying hybrid rocket fuels", Jan. 2003. DOI: 10.2514/6.2003-1162.

[10] S. Sisi and A. Gany, "Combustion of plain and reinforced paraffin with nitrous oxide", *International Journal of Energetic Materials and Chemical Propulsion*, vol. 14, no. 4, pp. 331–345, 2015. DOI: 10.1615/intjenergeticmaterialschemprop.2015011139.

[11] M. C. Tarifa and L. Pizzuti, "Theoretical performance analysis of hybrid rocket propellants aiming at the design of a test bench and a propulsive system", *8th European Conference for Aeronautics ans Space Sciences (EUCASS)*, 2019. DOI: 10.13009/EUCASS2019-488.

[12] A. Karabeyoglu, D. Altman, and B. Cantwell, "Combustion of liquefying hybrid propellants: Part 1, general theory", *Journal of Propulsion and Power - J PROPUL POWER*, vol. 18, May 2002. DOI: 10.2514/2.5975.

[13] G. Di Martino, S. Mungiguerra, C. Carmicino, and R. Savino, "Computational fluid-dynamic modeling of the internal ballistics of paraffin-fueled hybrid rocket", *Aerospace Science and Technology*, vol. 89, pp. 431–444, 2019. DOI: 10.1016/j.ast.2019.04.019.

[14] M. T. Migliorino, D. Bianchi, and F. Nasuti, "Numerical analysis of paraffin-wax/oxygen hybrid rocket engines", *Journal of Propulsion and Power*, vol. 36, no. 6, pp. 806–819, 2020. DOI: 10.2514/1.b37914.

[15] *Chemical equilibrium with applications, cea*. [Online]. Available: https://cearun.grc.nasa.gov/.

[16] A. E.-S. Makled and M. K. Al-Tamimi, "Hybrid rocket motor performance parameters: Theoretical and experimental evaluation", *International Journal of Aerospace and Mechanical Engineering*, vol. 11, no. 1, pp. 47–55, 2017, ISSN: eISSN: 1307-6892. [Online]. Available: https://publications.waset.org/vol/121.